ARTICLE

Higher-order assembly of Sorting Nexin 16 controls tubulation and distribution of neuronal endosomes

ShiYu Wang, Zechuan Zhao, and Avital A. Rodal

The activities of neuronal signaling receptors depend heavily on the maturation state of the endosomal compartments in which they reside. However, it remains unclear how the distribution of these compartments within the uniquely complex morphology of neurons is regulated and how this distribution itself affects signaling. Here, we identified mechanisms by which Sorting Nexin 16 (SNX16) controls neuronal endosomal maturation and distribution. We found that higher-order assembly of SNX16 via its coiled-coil (CC) domain drives membrane tubulation in vitro and endosome association in cells. In *Drosophila melanogaster* motor neurons, activation of Rab5 and CC-dependent self-association of SNX16 lead to its endosomal enrichment, accumulation in Rab5- and Rab7-positive tubulated compartments in the cell body, and concomitant depletion of SNX16-positive endosomes from the synapse. This results in accumulation of synaptic growth–promoting bone morphogenetic protein receptors in the cell body and correlates with increased synaptic growth. Our results indicate that Rab regulation of SNX16 assembly controls the endosomal distribution and signaling activities of receptors in neurons.

Introduction

Cells detect and respond to extracellular stimuli through cell-surface receptors. Ligand-bound receptors are internalized from the plasma membrane into the endosomal system, which is composed of a tubulovesicular network of polymorphic intracellular compartments. Receptors are transferred along this network in a spatially and temporally controlled manner to achieve different itineraries and specific signaling outputs (Rajendran et al., 2010; Cullen and Steinberg, 2018; Kaksonen and Roux, 2018). Neurons are highly sensitive to alterations in endosomal trafficking due to their compartmentalized morphology. The endocytic/endosomal system regulates neuronal growth and survival signaling via internalization and turnover of signaling receptors at synapses, as well as via long-distance axonal transport of receptor-containing endosomes to neuronal cell bodies (Deshpande and Rodal, 2016; Barford et al., 2017; Scott-Solomon and Kuruvilla, 2018). Regulation of these events depends on endosomal maturation, which is driven by changes in the lipid and protein composition of the endosome (Langemeyer et al., 2018).

Sorting Nexins (SNXs) are an important family of endosomal proteins, characterized by the presence of a phosphoinositide-binding Phox homology (PX) domain. SNXs participate in a variety of cellular processes, ranging from clathrin-mediated endocytosis to endosomal sorting and signaling to lipid metabolism (Cullen, 2008; Teasdale and Collins, 2012; Chandra and Collins,

2018). These diverse roles are achieved by coordination of the PX domain with their other functional domains (Honbou et al., 2007; Pylypenko et al., 2007; van Weering et al., 2012; Lucas et al., 2016; Chandra et al., 2019). However, the molecular and cellular mechanisms of many SNXs remain unexplored.

SNX16 has been implicated in regulating receptor traffic and signaling in both mammalian cells and *Drosophila melanogaster* (Hanson and Hong, 2003; Choi et al., 2004b; Rodal et al., 2011; Debaisieux et al., 2016). SNX16 contains a PX domain that binds specifically to phosphatidylinositol 3-phosphate (PI(3)P), as well as a C-terminal coiled-coil (CC) domain, which is required for its self-association in vivo (Hanson and Hong, 2003; Choi et al., 2004b; Chandra et al., 2019) and mediates dimerization in the SNX16 crystal structure (Xu et al., 2017). However, the mechanisms by which the CC domain contributes to the cellular functions of SNX16 are unknown. *Drosophila* SNX16 (dSNX16) promotes synaptic growth signaling via activated bone morphogenetic protein (BMP) receptors in presynaptic terminals at the neuromuscular junction (NMJ; Rodal et al., 2011). The F-BAR protein Nervous Wreck (Nwk) acts upstream of dSNX16 to constrain synaptic growth signaling, and this negative regulation is suppressed by mutating three highly conserved glutamates to alanines within the dSNX16 CC domain (Fig. 1 A; E347A, E350A, and E351A; hereafter referred to as dSNX16[3A]). Overexpression of dSNX16[3A] in *Drosophila* resulted in dramatic

Department of Biology, Brandeis University, Waltham, MA.

Correspondence to Avital A. Rodal: arodal@brandeis.edu.
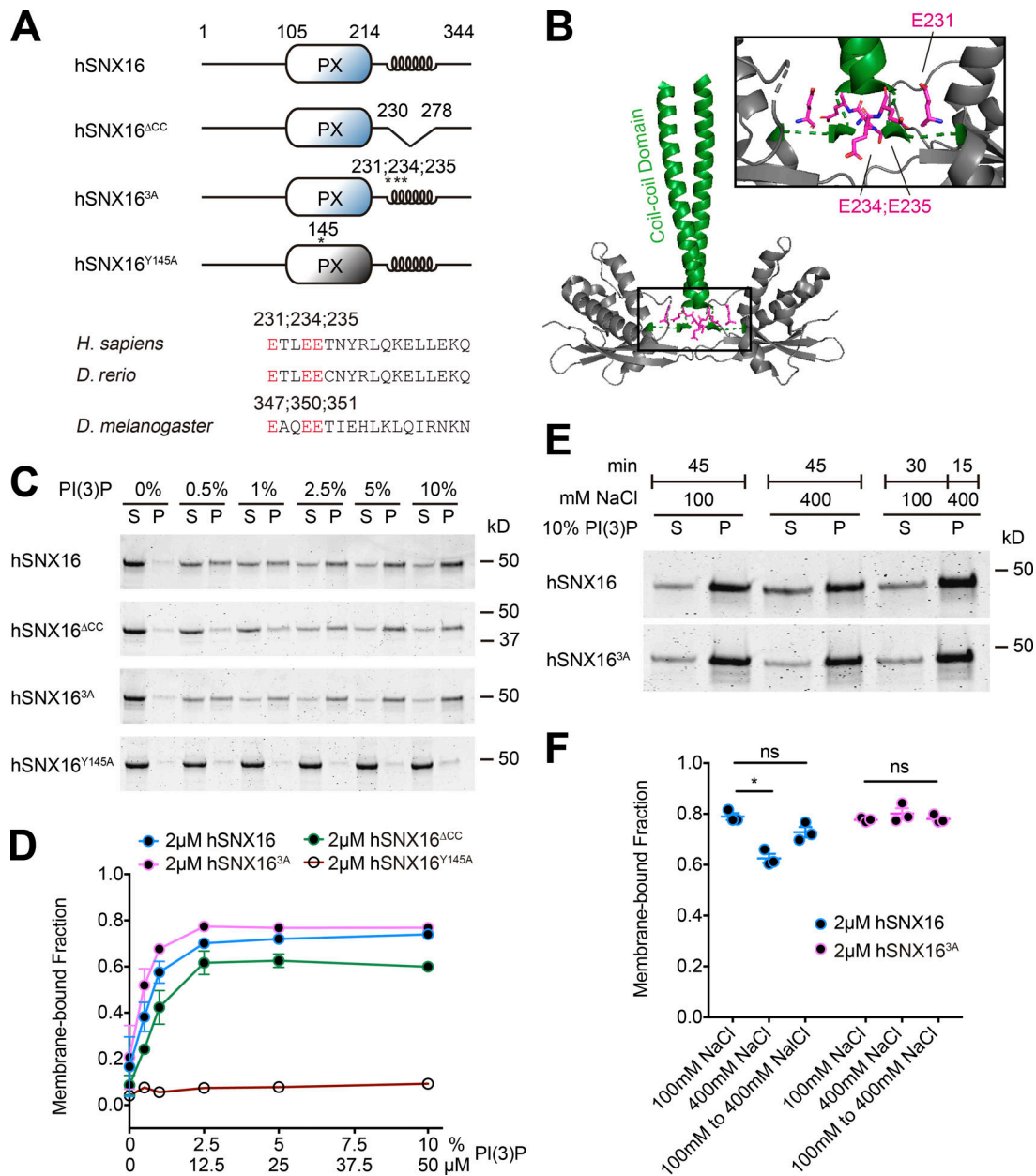
Figure 1. **PI(3)P-dependent lipid binding of hSNX16 CC domain mutants. (A)** Schematic of hSNX16 constructs. **(B)** Location of hSNX16 CC mutations on hSNX16 PX-CC dimer (PDB accession number 5GW0; Xu et al., 2017). CC domains are shown in green and glutamates in magenta. **(C–F)** Liposome cosedimentation assays. Purified hSNX16 variants were incubated with liposomes of the indicated composition and pelleted. Representative Coomassie staining of supernatant (S) and pellet (P) fractions is shown in C and E. **(C and D)** Liposomes composed of 80% DOPC (1,2-dioleoyl-sn-glycero-3-phosphocholine), 15% DOPE (1,2-dioleoyl-sn-glycero-3-phosphoethanolamine), 5% DOPS (1,2-dioleoyl-sn-glycero-3-phospho-L-serine), and PI(3)P (0.5%, 1%, 2.5%, 5%, and 10%; with a corresponding decrease in DOPC). PI(3)P-dependent lipid binding of purified hSNX16 CC domain mutants is not significantly different from wild-type hSNX16. Y145A mutation abolishes PI(3)P binding of hSNX16 as previously reported (Choi et al., 2004b). **(E and F)** Binding of wild-type hSNX16 is more salt sensitive than hSNX16[3A]. Liposomes (70% DOPC, 15% DOPE, 5% DOPS, and 10% PI(3)P) were incubated for 45 min with purified hSNX16 and the indicated NaCl concentrations before pelleting. In the last condition, hSNX16 and liposomes were incubated in 100 mM NaCl for 30 min, and then NaCl was added to a final concentration of 400 mM for 15 min before pelleting. Quantification is a result of three independent experiments, analyzed using a Kruskal–Wallis test followed by a Dunn's multiple comparisons test. Data are presented as mean ± SEM. *, $P < 0.05$. ns, not significant.

synaptic overgrowth and mislocalization of activated BMP receptors at the NMJ (Rodal et al., 2011), the opposite of the *dSnx16* loss-of-function phenotype, suggesting that dSNX16[3A] is dominant active. The mechanisms by which CC-dependent activities of dSNX16[3A] regulate neuronal endosomal traffic to promote signaling remain unclear.

Additional findings suggest an important role of the CC domain in SNX16 regulation. Human SNX16 (hSNX16) localizes to recycling and tubular late endosomes in addition to PI(3)P-rich early endosomes in immortalized cell lines (Hanson and Hong, 2003; Choi et al., 2004b; Le Blanc et al., 2005; Brankatschk et al., 2011; Zhang et al., 2013; Xu et al., 2017), suggesting that PI(3)P

binding is not sufficient to explain its endosome association. Deleting a fragment containing the CC domain results in hSNX16 loss from later endosomes and delays trafficking of internalized EGF (Hanson and Hong, 2003), highlighting the functional importance of the hSNX16 CC domain. Furthermore, the SNX16 PX domain and CC domain jointly contribute to the interaction with PI(3)P at the entrance to the PI(3)P-binding pocket (Xu et al., 2017). Interestingly, two of the three key residues from the CC domain (E234, E235, and Y238) shaping this entrance map to E350 and E351 in dSNX16, which are mutated in dominant-active mutant dSNX16[3A] (Fig. 1 B; Rodal et al., 2011; Xu et al., 2017).

In this study, we address the role of the SNX16 CC domain in regulating its molecular and cellular functions in vitro using purified proteins and synthetic liposomes and in vivo in cultured mammalian cells and *Drosophila* motor neurons.

Results

hSNX16 CC variants do not strongly affect PI(3)P binding

The structure of hSNX16 suggests that its CC domain could contribute to entrance of PI(3)P into the PX domain–binding pocket (Xu et al., 2017). To understand the role of the SNX16 CC domain in more detail, we purified wild-type hSNX16, a hSNX16 variant missing the full CC domain (hSNX16[ΔCC]), mutant hSNX16[3A] (E231A, E234A, and E235A), as well as a PX domain PI(3)P-binding pocket mutant hSNX16[Y145A] (Choi et al., 2004b) as a negative control (Fig. 1, A and B). We then tested PI(3)P binding of different CC variants in liposome cosedimentation assays (Fig. 1, C and D). Wild-type hSNX16 cosedimented more effectively with increasing PI(3)P concentration, and hSNX16[Y145A] abolishes PI(3)P binding, as previously shown (Choi et al., 2004b). By contrast, PI(3)P-binding sensitivities of hSNX16[ΔCC] and hSNX16[3A] were not significantly different from hSNX16 (Fig. 1 D), suggesting that the CC domain does not strongly modulate the lipid-binding affinity of SNX16.

We next tested if electrostatic interactions mediate the binding of hSNX16 and our CC variants to the membrane by conducting liposome cosedimentation assays in the presence of 400 mM NaCl. hSNX16 binding to 10% PI(3)P liposomes was reduced in the presence of NaCl. However, once bound to liposomes, hSNX16 was resistant to 400 mM NaCl, suggesting that the initial binding step is sensitive to electrostatic interactions, followed by more hydrophobically driven effects. Interestingly, though hSNX16[3A] exhibited similar lipid binding to hSNX16 at 10% PI(3)P, hSNX16[3A] binding was not sensitive to 400 mM NaCl (Fig. 1, E and F), suggesting that the CC domain may be involved in these hydrophobic interactions. These results raise the possibility that the CC domain of hSNX16 functions in parallel to the canonical PI(3)P-binding PX domain to mediate membrane association.

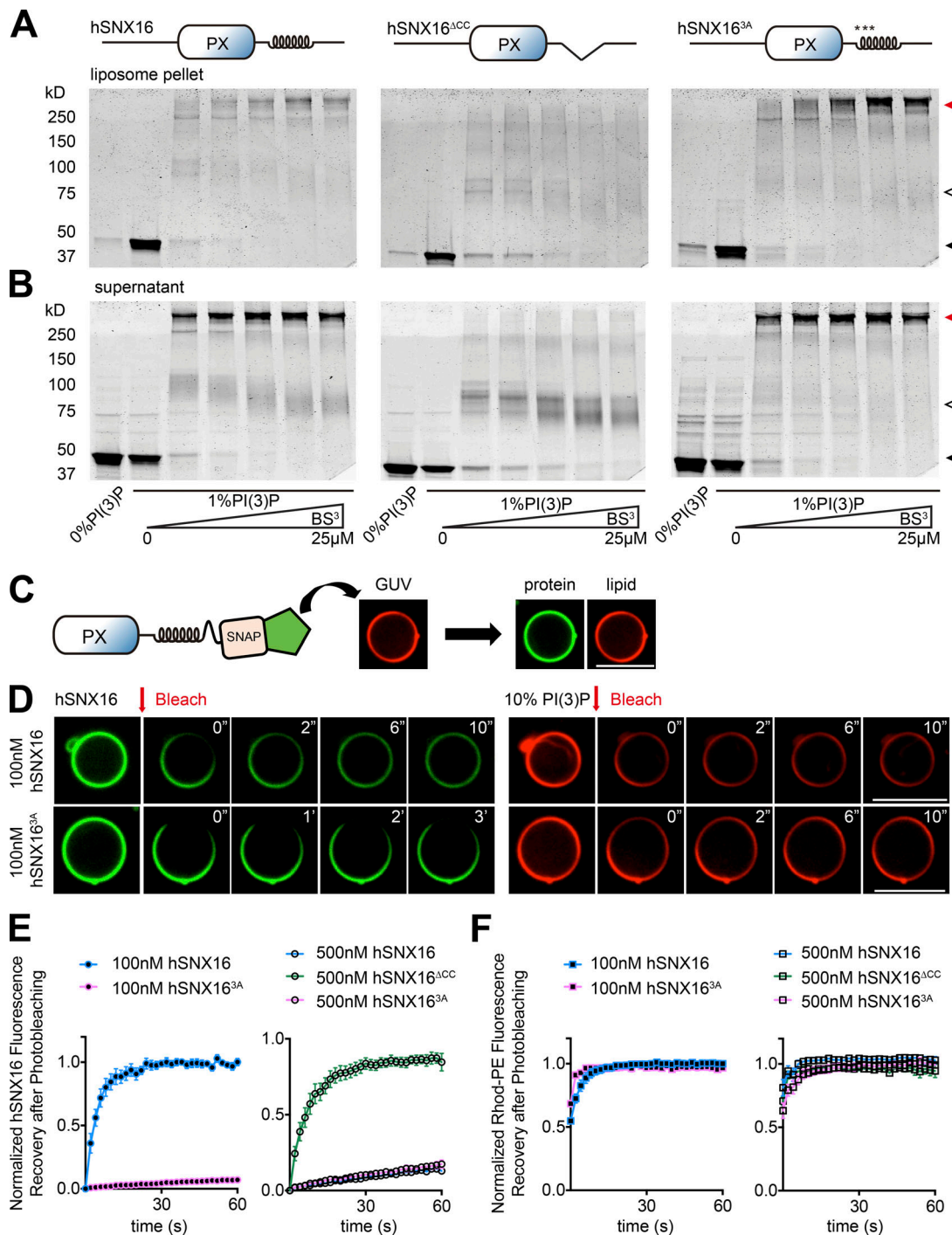### hSNX16 oligomerizes into higher-order assemblies via its CC domain

Since the hSNX16 CC domain mediates its homo-oligomerization (Hanson and Hong, 2003; Choi et al., 2004b), we hypothesized that altered salt sensitivity of hSNX16[3A] may be due to changes

in self-association. To test this hypothesis, we incubated hSNX16 CC variants with 1% PI(3)P liposomes and increasing concentrations of the 8-atom-long lysine cross-linker BS[3] and conducted cosedimentation assays (Fig. 2, A and B). In the liposome-containing pellet, hSNX16 formed cross-linked species at the molecular weight of dimers (~100 kD; Fig. 2, A and B, white triangle) as well as unexpected higher-order species (>200 kD; red triangle). hSNX16[ΔCC] produced minimal higher-order species, though we did observe dimers, consistent with previous findings that the PX domain contributes to self-association (Choi et al., 2004b). By contrast, hSNX16[3A] exhibited more abundant cross-linking than wild-type hSNX16 into higher-order species (Fig. 2 A), though total cosedimentation with PI(3)P was similar to hSNX16 and hSNX16[ΔCC] (Fig. S1, A and B). In the supernatant fraction, we also observed higher-order assemblies of hSNX16 and hSNX16[3A] and only dimer species of hSNX16[ΔCC] (Fig. 2 B). Interestingly, hSNX16[3A] supernatants lacked the dimer species and only showed higher-order assemblies. We then asked if these oligomers required the presence of membranes by conducting cross-linking assays in buffer alone. In contrast to liposome-containing cross-linking experiments, in the absence of liposomes, hSNX16 and hSNX16[3A] showed comparable dimer and higher-order assembly formation (Fig. S1 C), suggesting that oligomerization of hSNX16[3A] is potentiated by membranes. Taken together, we conclude that hSNX16 can oligomerize into higher-order assemblies via its CC domain and that hSNX16[3A], a mutant in the CC domain, promotes the formation of these assemblies.

To further explore hSNX16 higher-order assembly, we conducted FRAP experiments on giant unilamellar vesicles (GUVs) coated with SNAP[488]-labeled hSNX16 variants (Fig. 2 C). All hSNX16 variants coated GUVs uniformly and did not exhibit localized clustering. At 100 nM, hSNX16[3A] failed to recover after photobleaching a region of the GUV, while hSNX16 recovered rapidly (Fig. 2, D and E). At 500 nM, hSNX16 and hSNX16[3A] both failed to recover after photobleaching, while hSNX16[ΔCC] remained mobile, suggesting that hSNX16 higher-order assemblies form a stable scaffold on GUV via the CC domain and that the hSNX16[3A] mutant promotes these stable assemblies, consistent with our cross-linking results (Figs. 2 E and S1 D). In addition, labeled phosphatidyl-ethanolamine (PE) in the photobleached region recovered rapidly for all hSNX16 CC variants, indicating that this component of the membrane remained fluid even when the protein assembly did not (Fig. 2 F). Considering both the cross-linking and the GUV FRAP results, we conclude that hSNX16 can oligomerize into higher-order structures (beyond dimers) via its CC domain and that the hSNX16[3A] mutant and membrane binding together increase the formation of these oligomers.

hSNX16 higher-order assemblies promote membrane tubulation

When conducting the FRAP experiments with 500 nM hSNX16 variants, we consistently observed tubule formation on GUVs coated with hSNX16 and hSNX16[3A], but not hSNX16[ΔCC] (Fig. S1 D). This was unexpected, since SNX16 does not contain a Bin/Amphiphysin/Rvs167 (BAR)–domain scaffold like other membrane-tubulating SNXs (van Weering et al., 2012) and instead forms a

Figure 2. **hSNX16 oligomerizes into higher-order assemblies on membranes via its CC domain. (A and B)** hSNX16$^{\Delta CC}$ reduces and hSNX16^{3A} promotes self-association compared with hSNX16^{WT} on PI(3)P liposomes. 5 µM purified hSNX16, hSNX16^{3A}, or hSNX16$^{\Delta CC}$ were incubated with 1% (5 µM) PI(3)P liposomes followed by BS^3 cross-linking, and then tested for liposome cosedimentation. **(A)** Coomassie-stained gels of cross-linked high-molecular-weight assemblies in protein–liposome pellets with increasing BS^3 concentration (125 nM, 2.5 µM, 5 µM, 12.5 µM, and 25 µM). **(B)** Coomassie-stained gels of unbound proteins in the lipid cosedimentation assay from same experiments as in A. Black, white, and red triangles point to monomers, dimers, and higher-order assemblies, respectively. **(C)** Schematic of the GUV assay. **(D–F)** hSNX16^{3A} fails to recover after photobleaching at lower protein concentrations compared with wild-type hSNX16, while hSNX16$^{\Delta CC}$ retains high mobility at all concentrations measured. **(D)** Representative time-lapse images of 100 nM hSNX16 and hSNX16^{3A} before and after photobleaching. **(E and F)** Quantification of protein and lipid fluorescence of GUVs bound by hSNX16 variants at 100 nM and 500 nM. Protein and lipid fluorescence were normalized to a nonbleached region on the same GUV to correct for photobleaching. Protein fluorescence was then further normalized by subtracting from all time points the intensity at t = 0 and normalizing prebleach intensity to 1. Quantification is from five GUVs incubated with 100 nM hSNX16; six GUVs incubated with 100 nM hSNX16^{3A}, 500 nM hSNX16, or 500 nM hSNX16$^{\Delta CC}$; and eight GUVs incubated with 500 nM hSNX16^{3A}. Data are presented as mean ± SEM. Scale bars, 10 µm.
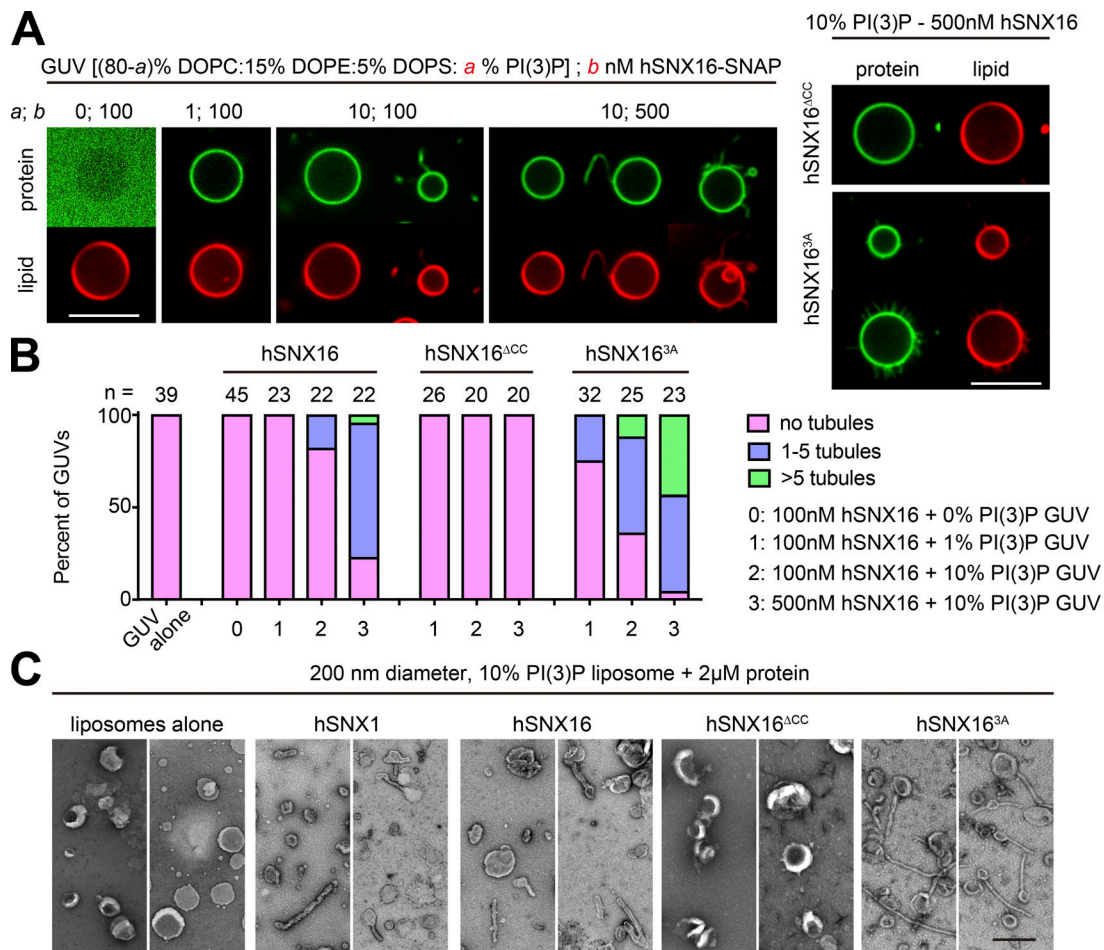
Figure 3. **hSNX16 generates membrane tubules via its CC region. (A)** Representative single confocal slices of rhodamine PE–labeled GUVs (0%, 1% [30 nM], or 10% [300 nM] PI(3)P) incubated with 100 nM or 500 nM hSNX16 CC variants. Scale bars, 10 µm. **(B)** Percentage of tubulated vesicles at the indicated PI(3)P and hSNX16 concentrations. Quantification is from at least 20 GUVs per condition. **(C)** Negative-stain EM of liposomes incubated with buffer, hSNX1, or hSNX16 CC variants (2 µM final protein concentration). Two representative fields are shown for each condition. Scale bar, 400 nm.

scissor-shaped homodimer (Xu et al., 2017). To investigate this novel membrane tubulation activity of hSNX16, we incubated hSNX16 CC variants with GUVs of various PI(3)P compositions and quantified GUV morphology (Fig. 3, A and B). We did not observe tubules on 0% PI(3)P GUVs incubated with hSNX16 or on GUVs without protein. By contrast, hSNX16 generated tubules on 10% PI(3)P GUVs at 100 nM, and the number of tubulated GUVs increased at 500 nM hSNX16 (Fig. 3, A and B). Notably, hSNX16[3A] generated tubules at lower PI(3)P and protein concentrations than hSNX16, and hSNX16[ΔCC] failed to generate tubules under any tested conditions (Fig. 3, A and B). Thus, the tubulation activity of hSNX16 and our CC variants correlated with their capability to form higher-order assemblies in cross-linking and FRAP assays.

Because GUVs are cell-sized vesicles that are essentially flat at the scale of individual proteins, we next tested whether hSNX16 promotes membrane tubulation on smaller, endosome-size vesicles using negative-stain EM. After incubation with 200 nm liposomes, hSNX16 and hSNX16[3A] exhibited tubulation comparable to the BAR domain–containing SNX1 (Fig. 3 C), while hSNX16[ΔCC] did not exhibit tubulation. Thus, hSNX16 generates membrane tubules via its CC domain, and this membrane

tubulation activity correlates with higher-order assembly. Taken together, our in vitro data indicate that the CC domain is required for hSNX16 higher-order assembly and membrane-deforming activities and that the hyperoligomerized mutant hSNX16[3A] promotes these activities.

hSNX16 CC variants control endosome association in vivo

To investigate the importance of hSNX16 oligomerization in vivo, we next tested the subcellular localization of hSNX16 CC variants in cells. hSNX16 exhibited both punctate and cytoplasmic localization, and some puncta were elongated or tubulated, as previously reported (Fig. 4; Choi et al., 2004b; Brankatschk et al., 2011; Xu et al., 2017). One previous study found that deletion of a hSNX16 fragment longer than but including the CC domain (aa 214–295) resulted in its loss from late endosomes while preserving early endosome localization in A431 cells (Hanson and Hong, 2003). We further found that a more precise deletion of the CC domain (aa 230–278) resulted in partial loss of hSNX16 from punctate structures and net redistribution to the cytoplasm in cultured rat hippocampal neurons (Fig. 4 A). In contrast, hSNX16[3A] exhibited enhanced punctate
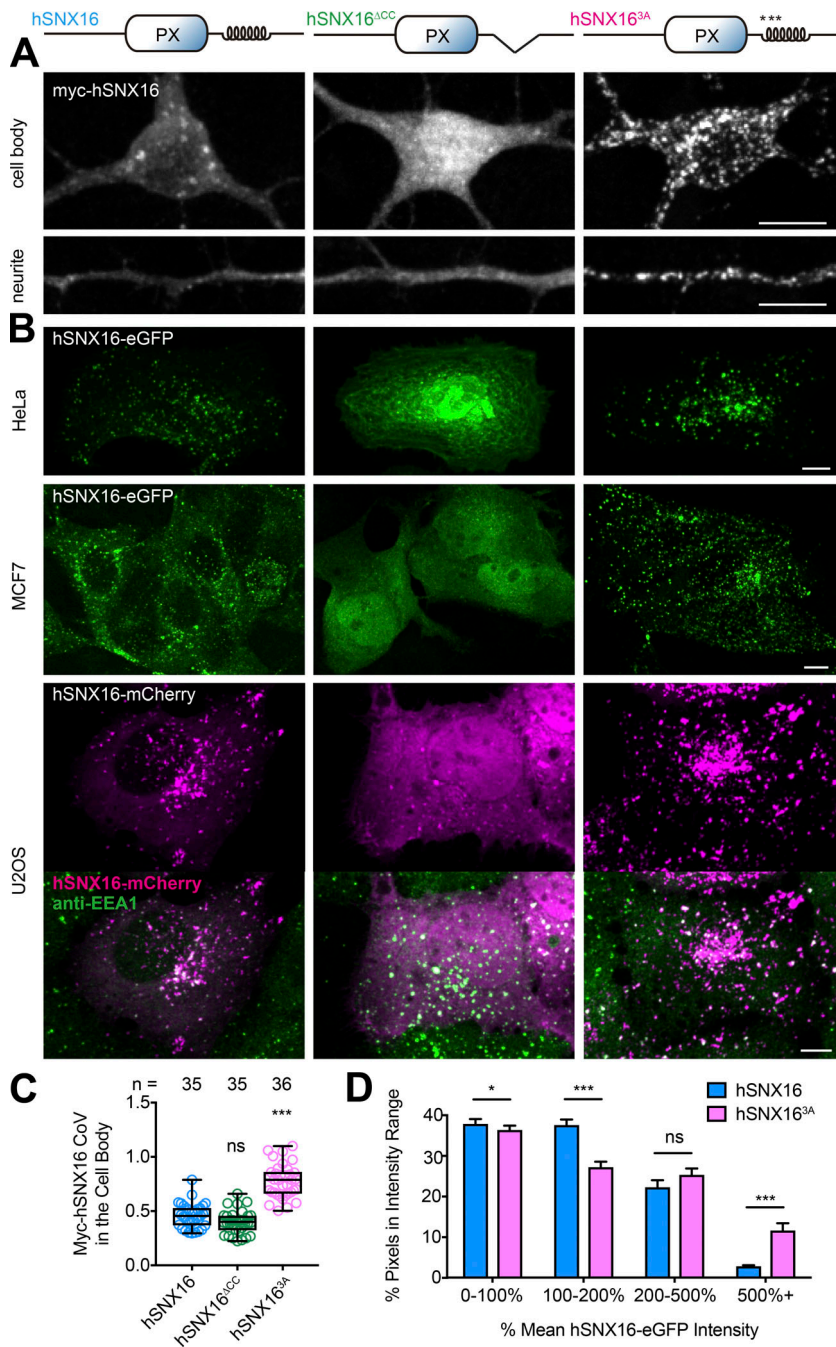
Figure 4. **hSNX16 CC mutants exhibit altered subcellular localization in vivo.** hSNX16$^{\Delta CC}$ reduces and hSNX16^{3A} enhances hSNX16 punctate localization in mammalian cells. **(A)** Representative images of cell body and neurites from immunostained DIV 7 rat hippocampal neurons transiently expressing the indicated myc-hSNX16 variants. **(B)** Representative images of the indicated cell lines expressing indicated hSNX16 CC variants and fixed 24 h after transfection. hSNX16-transfected U2OS cells were stained with α-EEA1 antibodies. **(C)** CoV (standard deviation/mean of pixel intensities) of myc-hSNX16 CC mutants in hippocampal cell bodies. Quantification is from ≥35 neurons per condition from three independent coverslips, tested for normality and analyzed using a one-way ANOVA followed by Tukey's test. **(D)** Histograms depict fraction of pixels at the indicated intensities for hSNX16 and hSNX16^{3A} in HeLa cells. Quantification is from 14 cells per condition and analyzed using a Mann–Whitney U test within each bin. All images show 2D maximum intensity projections of confocal stacks. Data are shown as box-and-whisker plots with all data points superimposed in C and as mean + SEM in D. *, $P < 0.05$; ***, $P < 0.001$. ns, not significant. Scale bars, 10 µm.

localization and was depleted from the cytosol. To understand whether this subcellular localization of hSNX16 CC variants is unique to neurons, we tested multiple mammalian cell lines and observed similar results, suggesting a general role for CC domain–promoted oligomerization in hSNX16 endosomal localization (Fig. 4 B). Further, the puncta found in all hSNX16 CC variants partially colocalized with early endosome antigen 1 (EEA1), consistent with previous findings that SNX16 distributes among early and late endosomes (Choi et al., 2004b; Brankatschk et al., 2011; Xu et al., 2017). We further quantified the change in hSNX16^{3A} subcellular localization and found that it was significantly more clustered than hSNX16, as measured both by an increase at the neuronal cell body of coefficient of variation (CoV; or standard deviation/mean intensity, reflecting a nonuniform distribution of pixel intensities), as well as a larger fraction of high-intensity pixels in HeLa cells (Fig. 4, C and D). Thus, we conclude that the hSNX16 CC domain is required for its proper endosomal localization in vivo and that the hSNX16^{3A} mutant, which exhibits enhanced oligomerization in vitro, also promotes hSNX16 endosome localization.

dSNX16 CC variants control localization and tubulation of compartments in *Drosophila* motor neurons

Previously, we reported that null mutants of *dSnx16* cause reduced synaptic growth at the *Drosophila* NMJ and that *dSnx16*^{3A} acts as a dominant-active mutant and exhibits a synaptic

overgrowth phenotype (Rodal et al., 2011). We therefore examined how the SNX16 CC-mediated oligomerization behavior that we observed in the mammalian system could contribute to its functional role at the *Drosophila* NMJ. We first tested whether the in vivo change in subcellular localization that we observed in mammalian cells is conserved. We generated transgenic fly lines with SNAP-tagged dSNX16 CC variants, each inserted into the same genetic locus, and used the binary GAL4/UAS system to examine their localization upon expression in *Drosophila* larval motor neurons. This allowed us to examine localization within different neuronal structures, including cell bodies and dendrites in the ventral ganglion, axons bundled in segmental nerves, and NMJ axon terminals embedded at the surface of the muscle (see Fig. S2 A for a schematic). dSNX16 primarily localized to punctate structures at the NMJ (Fig. 5 A), which, as we previously described, correspond to endosomes (Rodal et al., 2011). Further, we found that similar to hSNX16 localization in mammalian cells, dSNX16 exhibited both cytoplasmic and punctate localization in axons proximal to the ventral ganglion, as well as in the cell bodies. Deletion of the dSNX16 CC domain resulted in increased cytoplasmic localization, while dSNX16³ᴬ exhibited enhanced punctate localization, similar to our observations for hSNX16 (Fig. 5, A and C), indicating that the function of the CC domain in SNX16 localization is conserved. Furthermore, via structured illumination microscopy (SIM) of neuronal cell bodies, we found that dSNX16 localized to tubulated structures (Fig. 5 B). This tubule localization was CC domain dependent, and an increased number of tubulated compartments were observed in the cell body of dSNX16³ᴬ-expressing animals, correlating with the tubulation activity of hSNX16 CC variants in vitro. We next measured the intensity of dSNX16 CC variants at the NMJ, proximal axon, and cell body and found that dSNX16³ᴬ was specifically enriched at the cell body, while dSNX16^ΔCC exhibited overall decreased intensity (Fig. 5 D). The enhanced punctate localization and cell body enrichment of dSNX16³ᴬ was also observed for randomly integrated UAS-dSNX16-GFP P-element lines with different expression levels (Fig. S2, B–D; Rodal et al., 2011). These results suggest that in *Drosophila* motor neurons, where SNX16 positively regulates synaptic growth signaling, dSNX16 CC variants control the abundance, distribution, and structure of endosomes.
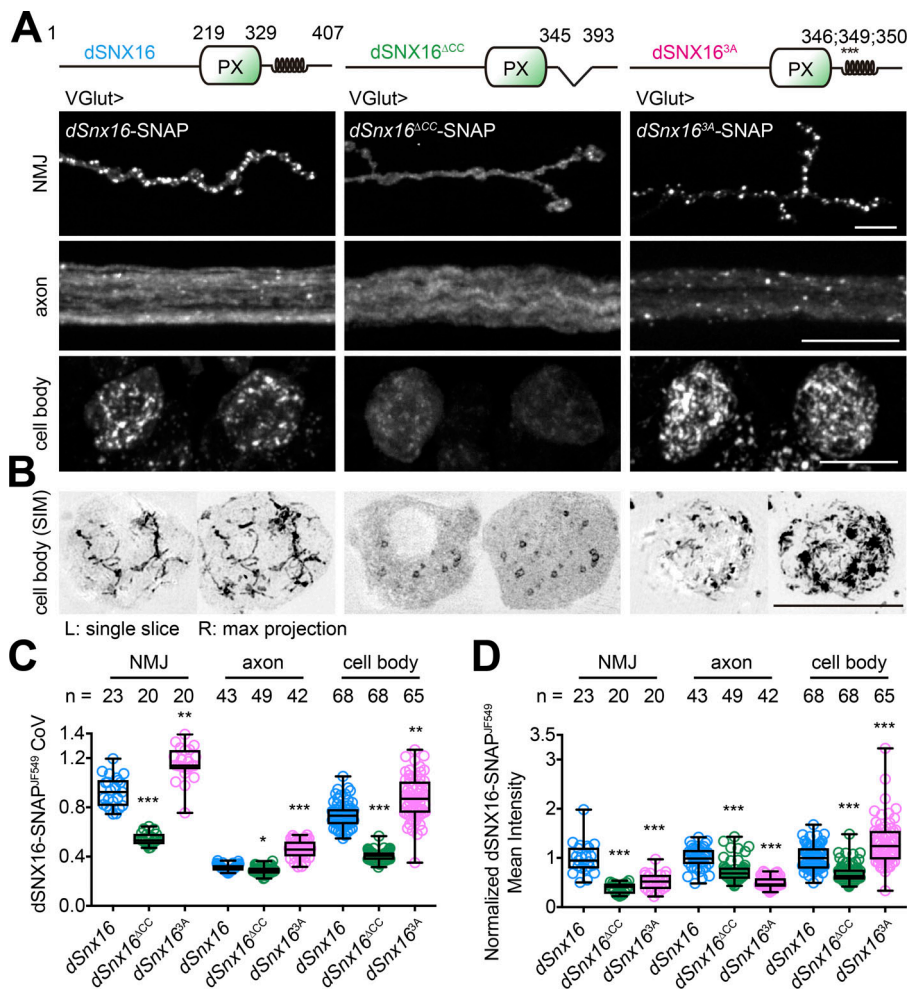
dSNX16 CC variants alter BMP receptor localization and signaling

dSNX16 colocalizes with and controls the activity of the BMP signaling pathway receptor Thickveins (Tkv) at the NMJ (Rodal et al., 2011). To understand the functional relevance of the altered distribution of dSNX16 CC variants, we examined their effects on BMP-dependent synaptic growth. We previously found that NMJ signaling by a constitutively active BMP receptor (Tkv^Q199D; Hoodless et al., 1996) was highly sensitive to the SNX16 pathway (Rodal et al., 2011). We expressed Tkv^Q199D in motor neurons together with dSNX16 CC variants in an otherwise wild-type background and found that both dSNX16³ᴬ and (to a lesser extent) dSNX16^ΔCC caused an increased number of boutons relative to controls (Fig. 6 A). We further measured the

levels of phosphorylated Mad (pMad), a downstream target of the BMP pathway that translocates into nuclei upon activation (Marqués et al., 2002; McCabe et al., 2003; Rawson et al., 2003), and found that both dSNX16³ᴬ and dSNX16^ΔCC led to elevated pMad in motor neuron nuclei compared with wild-type dSNX16 (Fig. 6, B and C).

How could both tubulating and nontubulating forms of dSNX16 promote synaptic growth, and how does this relate to their subcellular distribution? To answer these questions, we first examined the colocalization of dSNX16 and mCherry-tagged Tkv throughout the neuron (Fig. 6, D and E). Wild-type dSNX16 partially colocalized with Tkv in fixed cell bodies, axons, and NMJs (Fig. 6 D). To explore the relationship between dSNX16 and Tkv in different parts of the neuron, we examined their transport by live imaging of axons (Fig. 6 E and Videos 1 and 2). Most Tkv particles are motile in both directions, as we and others previously described (Smith et al., 2012; Kang et al., 2014; Deshpande et al., 2016). In 11 (4-min) recordings from eight animals, we counted 136 dSNX16-positive particles (66.2% stationary, 11.7% anterograde, and 22.1% retrograde). We observed only 13 cotransporting dSNX16 and Tkv particles. 10 out of 13 of these particles moved in the retrograde direction, and 3 out of 13 were stationary, indicating that dSNX16-Tkv particles are biased to motility in the retrograde direction relative to dSNX16-only particles. These results are consistent with the idea that SNX16 transits from the NMJ to the cell body with cargo but do not rule out that Tkv may accumulate on SNX16 endosomes in the cell body independent of retrograde endosome transport.

We then examined the colocalization of Tkv-mCherry and dSNX16 CC variants. Interestingly, despite our observation that dSNX16^ΔCC-SNAP was expressed at overall lower levels and had higher diffuse signal relative than dSNX16 (Fig. 5, C and D) and that overall Tkv levels were reduced at dSNX16^ΔCC-expressing cell bodies, we found that dSNX16^ΔCC had a similar Pearson correlation coefficient (PCC) to wild-type dSNX16 with Tkv-positive endosomes in the cell body and axon (Fig. 6 F). This result suggests that Tkv is enriched in dSNX16^ΔCC-positive endosomes in the cell body relative to the rest of the neuron. dSNX16³ᴬ-SNAP colocalization with Tkv was strongly increased compared with wild-type SNX16, concomitant with increased Tkv intensity at the cell body and axon (Fig. 6, F and G), the opposite effect from dSNX16^ΔCC. We corroborated these results using two different dSNX16³ᴬ-GFP lines (to control for the effects of expression levels) and found that the stronger dSNX16³ᴬ-GFP line also exhibited enhanced colocalization with Tkv and Tkv accumulation at the NMJ, proximal axon, and cell body compared with wild-type dSNX16-GFP, while the weaker dSNX16³ᴬ-GFP line only promoted Tkv accumulation in the cell body (Fig. S3, A–C). These results suggest that BMP signaling components in the cell body are most sensitive to the effects of dSNX16³ᴬ. We therefore used SIM to examine Tkv localization within dSNX16-coated endosomes in the cell body and observed that although Tkv was found in the vacuolar compartment of dSNX16- or dSNX16³ᴬ-positive endosomes, it was strikingly absent from dSNX16- or dSNX16³ᴬ-decorated tubules (Fig. 6 H, arrowheads). Taken together, our results indicate that dSNX16

Figure 5. **dSNX16 CC variants alter endosome structure, localization, and distribution in larval motor neurons. (A and B)** Representative images of animals expressing indicated UAS-dSnx16-SNAP variants driven by VGlut-GAL4. Shown are muscle 4 NMJ, proximal axons (within 100 μm of the ventral ganglion), and MNISN-I cell bodies (motor neuron in the intersegmental nerve I [Choi et al., 2004a]; see Fig. S2 A for schematics). dSNX16ΔCC reduces and dSNX16³ᴬ enhances dSNX16 punctate localization. dSNX16³ᴬ levels are increased at the cell body and reduced at the NMJ. **(B)** dSNX16 localizes tubular structures at the cell body revealed by SIM. dSNX16ΔCC reduces and dSNX16³ᴬ increases the quantity of tubulated SNX16 compartments. **(C and D)** CoV and mean intensity quantification of dSNX16-SNAPᴶᶠ⁵⁴⁹. Quantification is from ≥20 NMJs, 42 axons, or 65 cell bodies and analyzed using a Kruskal–Wallis test followed by Dunn's multiple comparisons test. Intensities were normalized to the mean intensity in the wild-type dSNX16 condition. All images show 2D maximum intensity projections of confocal stacks unless noted otherwise. Data are shown as box-and-whisker plots with all data points superimposed. *, $P < 0.05$; **, $P < 0.01$; ***, $P < 0.001$. Scale bars, 10 μm.

CC variants promote Tkv traffic and BMP signaling by altering endosomal localization and cell body levels of Tkv by different mechanisms.

We then asked whether the effects of dSNX16 CC variants on Tkv are specific to this cargo or could be generalized to other cargoes by examining the distribution of exogenously expressed human Transferrin receptor (hTfR; Fig. S3 D). We found that motor neuron–expressed hTfR localizes to puncta in the cell body and NMJ and also traffics into postsynaptic structures that are likely to be endosome-derived exosomes (Korkut et al., 2009, 2013), which is consistent with previous descriptions of transferrin receptor as a canonical exosome cargo (Pan and Johnstone, 1983). We found an increased colocalization of hTfR with dSNX16³ᴬ and decreased colocalization with dSNX16ΔCC in the cell body, consistent with the levels and distribution of dSNX16 variants in these compartments (Fig. 5, C and D). However, we found no changes in overall levels of hTfR in the cell body or NMJ, suggesting that the effect on Tkv levels is specific (Fig. S3, E and F).

dSNX16 association with endosomal compartments differs between the NMJ and cell body
Our results indicate that the dSNX16 CC variants may have distinct effects on endosomes in different regions of neurons.

To further understand the nature of dSNX16 puncta in these regions, we examined the colocalization of dSNX16 with previously described dSNX16-associated markers Rab5 (early endosomes), Rab7 (late endosomes), and Rab11 (recycling endosomes) in the cell body, axon, and NMJ (Fig. 7, A and B; and Fig. S4, A and B), using endogenously tagged Rabs or antibodies, to avoid effects of overexpressing tagged transgenes. However, we could not measure colocalization between dSNX16 with Rab5, Rab7, or Rab11 in axons, since unlike the NMJ and cell body, we could not segment the motor neurons in which dSNX16 was expressed away from the many additional cell types in the nerve bundle in which endogenous Rab proteins are found (Fig. S4 B). As we previously reported (Rodal et al., 2011), at the NMJ, we found dSNX16 localized to Rab5-positive early endosomes (Fig. 7, A and C). Here we report that at the NMJ, dSNX16 colocalized poorly with Rab7-positive late endosomes. By contrast, in the cell body, dSNX16 localized to both Rab5-positive and Rab7-positive puncta, suggesting different maturation states of dSNX16 containing endosomes at the nerve terminal compared with the cell body (Fig. 7, B and D). dSNX16 did not specifically colocalize with Rab11 in puncta in any region of the neuron, although strong diffuse Rab11 signal at the NMJ may produce an artificially high PCC (Fig. 7, C and D; and Fig. S4 A).
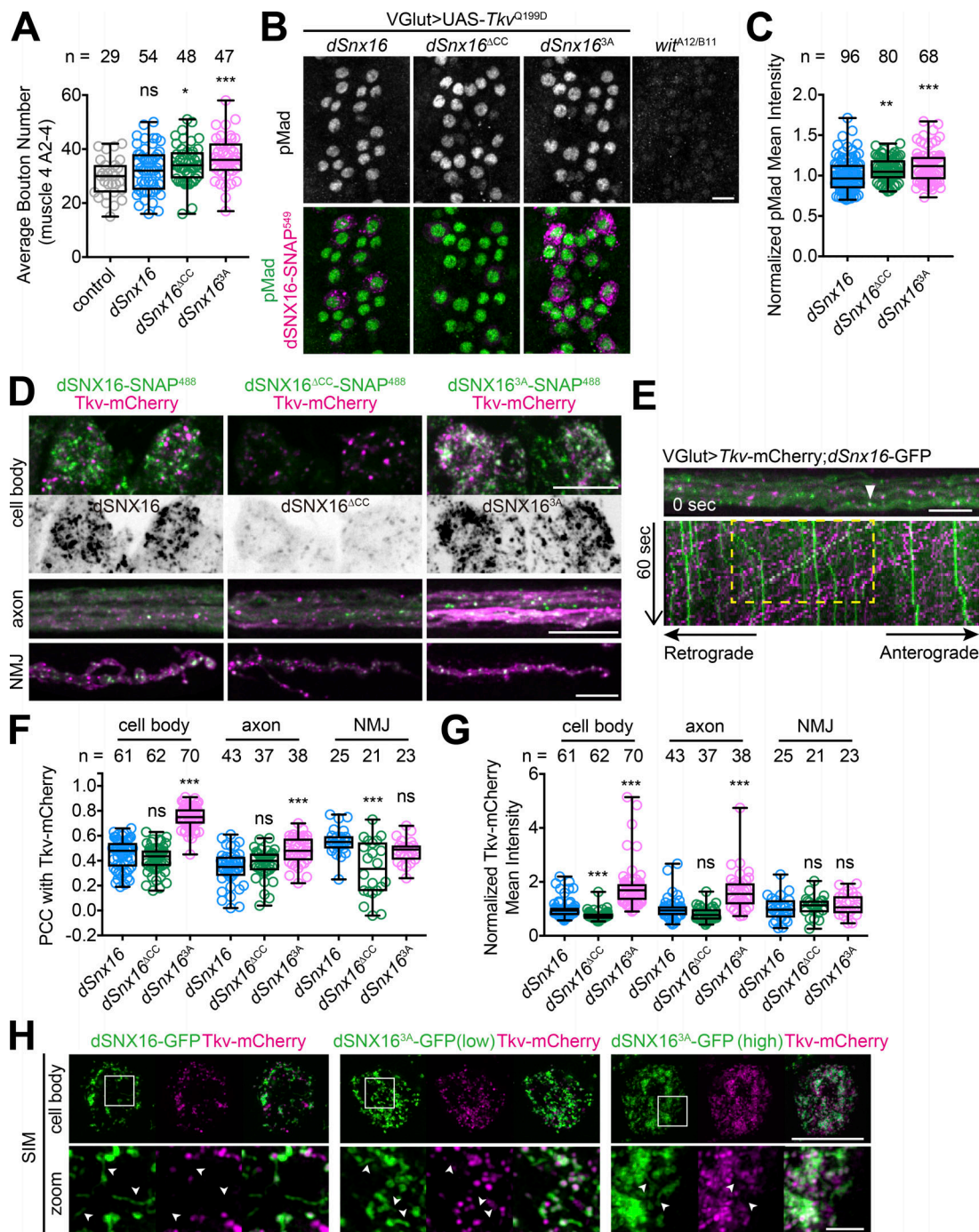
Figure 6. **dSNX16 CC variants regulate endosomal localization of Tkv to promote BMP signaling. (A)** Quantification of the mean bouton number on muscle 4 in animals expressing VGlut-driven UAS-Tkv^{Q199D} and UAS-$dSnx16$-SNAP variants. **(B)** Representative images of α-pMad–stained animals expressing VGlut-driven Tkv^{Q199D} and $dSnx16$-SNAP variants in the ventral nerve cords. **(C)** Quantification of pMad intensity measured from single, central slices of dSNX16-positive cell bodies. **(D)** Representative images of animals expressing VGlut-driven Tkv-mCherry and $dSnx16$-SNAP variants at the muscle 4 NMJ, proximal axon, and cell body. **(E)** Representative axonal transport kymograph of VGlut-driven Tkv-mCherry and $dSnx16$-GFP (corresponds to Video 1). Arrowhead indicates a dSNX16 particle containing Tkv, and yellow box highlights the retrograde movement of this particle over time. **(F)** PCCs between Tkv-mCherry and dSNX16 CC variants. **(G)** Mean intensity quantification of Tkv-mCherry. **(H)** Representative SIM images of animals expressing VGlut-driven Tkv-mCherry and the indicated dSNX16-GFP in the cell body. dSNX16³ᴬ-GFP (low) and dSNX16³ᴬ-GFP (high) lines correspond to dSNX16³ᴬ-GFPIIA and dSNX16³ᴬ-GFPIIIF lines in Fig. S2. Arrowheads indicate tubular dSNX16 compartments that do not contain Tkv. Quantification is from ≥21 NMJs, 37 axons, or 61 cell bodies analyzed using Kruskal–Wallis tests followed by Dunn's multiple comparisons test. All intensity measurements were normalized to mean intensity in the wild-type dSNX16 condition. All images show 2D maximum intensity projections of confocal stacks. Data are shown as box-and-whisker plots with all data points superimposed. *, P < 0.05; **, P < 0.01; ***, P < 0.001. ns, not significant. Scale bars, 10 µm; or 2 µm in the zoomed-in view of H.

Wang et al.
Regulation of neuronal membrane traffic by SNX16

Journal of Cell Biology
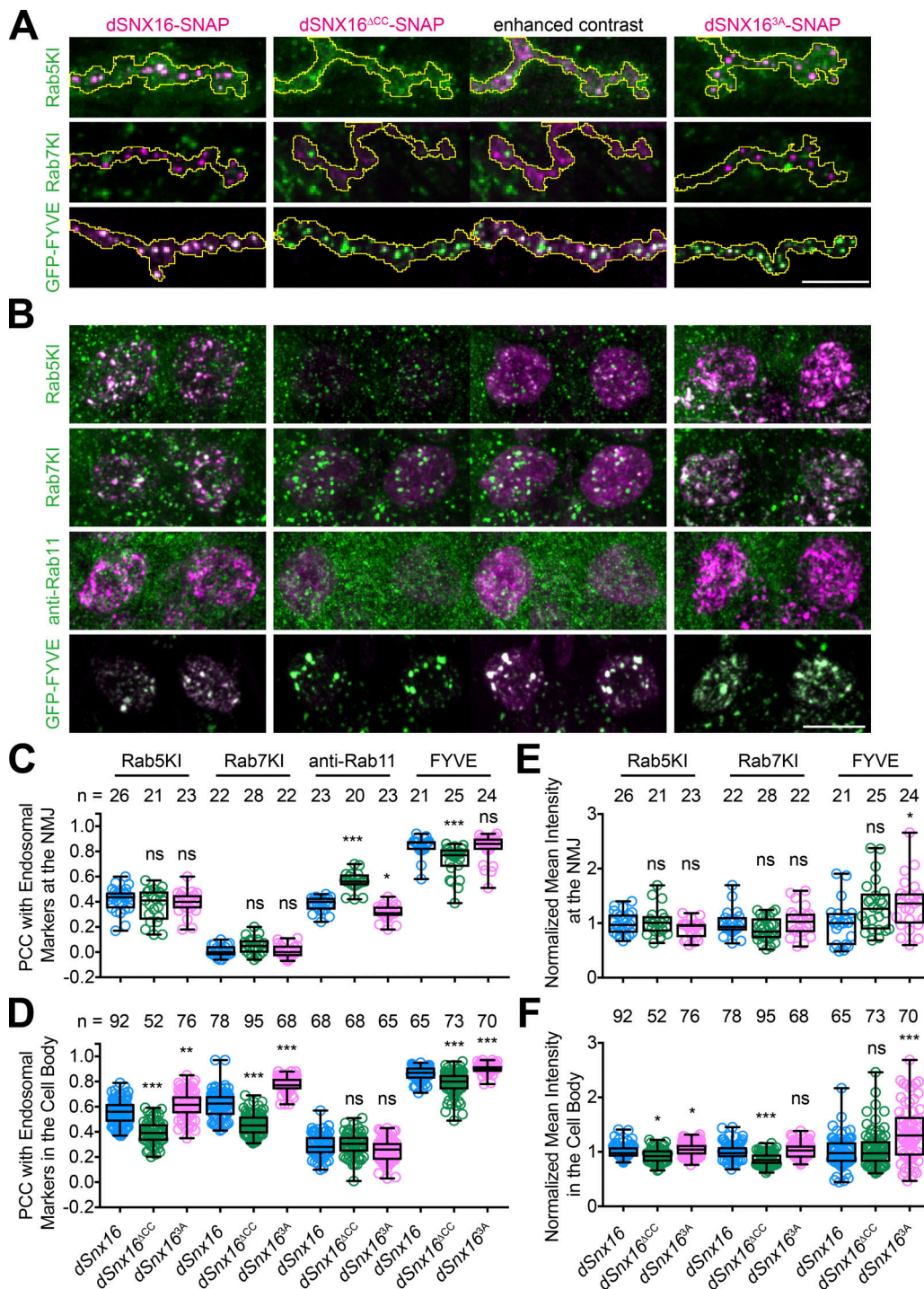https://doi.org/10.1083/jcb.201811074

2608

Figure 7. **The dSNX16 CC domain regulates its endosomal localization specifically in the cell body. (A and B)** Representative images of animals expressing VGlut-GAL4–driven *dSnx16*-SNAP transgenes. **(C)** PCCs between dSNX16 and Rab5, Rab7, α-Rab11 immunoreactivity, or UAS-GFP-myc-2xFYVE at the NMJ. **(D)** PCC between dSNX16 and endogenous GFP-Rab5, YFP-Rab7, α-Rab11 immunoreactivity, or UAS-GFP-myc-2xFYVE in the cell body. **(E)** Mean intensity quantification of Rab5, Rab7, and FYVE at the NMJ. **(F)** Mean intensity quantification of Rab5, Rab7, and FYVE in the cell body. Quantification is from ≥21 NMJs or 52 cell bodies, analyzed using a Kruskal–Wallis test followed by Dunn's multiple comparisons test. Intensity measurements were normalized to mean intensity in the wild-type dSNX16 condition. All images show 2D maximum intensity projections of confocal stacks. Data are shown as box-and-whisker plots with all data points superimposed. *, $P < 0.05$; **, $P < 0.01$; ***, $P < 0.001$. ns, not significant. Scale bars, 10 µm.

We then examined the colocalization of dSNX16 CC variants with Rab-marked endosomes. In the cell body, dSNX16$^{\Delta CC}$ colocalized more poorly than wild-type dSNX16 with Rab5 and Rab7 (Fig. 7, B and D). By comparison, at the NMJ, dSNX16$^{\Delta CC}$ colocalized with Rab5 similarly to wild-type dSNX16, suggesting that it may actually be enriched on NMJ early endosomes

relative to its distribution elsewhere (Fig. 7, A and C). By contrast, dSNX16[3A] exhibited increased colocalization in the cell body with Rab5-positive endosomes and to an even greater extent with Rab7-positive endosomes relative to wild-type dSNX16. These CC-dependent changes in dSNX16 association with Rab7-positive endosomes were not observed at the NMJ, where both dSNX16 and dSNX16[3A] similarly reside on Rab5-positive endosomes (Fig. 7, A–D).

We then asked if expression of these dSNX16 variants affected the distribution of specific types of endosomes within the neuron. dSNX16[ΔCC] caused a modest loss of Rab5 and Rab7 from the cell body. By contrast, dSNX16[3A] promoted a modest accumulation of Rab5, but not Rab7, in the cell body. Neither CC variant had any effect at the NMJ (Fig. 7, E and F). Thus, while dSNX16 CC variants do not dramatically change the distribution of endosomes in the cell body, it is interesting to note that dSNX16[3A] and dSNX16[ΔCC] did have significant and opposite effects.

Finally, we examined colocalization of dSNX16 variants with GFP-myc-2xFYVE (FYVE), a reporter for PI(3)P-rich endosomal compartments. Expression of FYVE abrogated our previously observed accumulation of dSNX16[3A] relative to wild-type dSNX16 in the cell body (Fig. S4 C), suggesting it may not be behaving as a completely inert biosensor (Wills et al., 2018). Given this caveat, FYVE colocalized with dSNX16 CC variants similarly to Rab5 at the NMJ and cell body (Fig. 7, C and D). Since dSNX16 and FYVE were both expressed using the GAL4-UAS system in motor neurons, we could examine their colocalization in axon bundles and found strong association with all CC variants (Fig. S4 E). Interestingly, dSNX16[3A] caused an increase in overall FYVE levels in both the cell body and NMJ, as well as increased FYVE CoV in the cell body (Fig. 7, E and F; and Fig. S4 F), suggesting that it may prevent endosome maturation to such an extent that the reporter itself is stabilized and accumulates to high levels. For dSNX16[ΔCC], we observed an increase in CoV with no change in total levels of FYVE in the cell body, axon, or NMJ (Fig. 7, E and F; and Fig. S4, D and F), arguing that dSNX16[ΔCC] endosomes are enriched for PI(3)P, indicative of altered endosome maturation but with different consequences for endosome distribution compared with dSNX16[3A].

Rab5 activates dSNX16 endosome association, distribution, and remodeling in vivo

Our previous observation that dSNX16[3A]-expressing animals exhibit synaptic overgrowth, opposite from the effects of dSnx16 null mutants, suggests that dSNX16[3A] is a dominant-active mutant (Rodal et al., 2011). Further, our in vitro data indicate that SNX16[3A] potentiates the normal oligomerization and membrane tubulation activity of SNX16 and does not behave as a neomorphic gain of function. Therefore, we hypothesized that there may be mechanisms in vivo to activate dSNX16 toward a more dSNX16[3A]-like behavior for endosome association and deformation. We tested whether manipulations of Rab5 or Rab7 could activate dSNX16 based on our colocalization results with these GTPases. Strikingly, similar to dSNX16[3A]-expressing animals, overexpressing a constitutively active Rab5 transgene (Rab5[CA]) enhanced wild-type dSNX16-GFP punctate localization at the

proximal axon (where this phenotype is highly robust; Fig. S2 D) and concomitantly enriched dSNX16 in the cell body (Fig. 8, A–C). By contrast, in Rab5[DN]-expressing animals, dSNX16 exhibited primarily cytoplasmic localization, which is the opposite of dSNX16[3A]- and Rab5[CA]-expressing animals (Figs. 8 B and S5 A). dSNX16 levels were also elevated in all compartments in Rab5[DN]-expressing animals.

Next, since dSNX16 in Rab5[CA]-expressing animals exhibited dSNX16[3A]-like behaviors, we tested whether Rab5 can also modulate dSNX16 tubule localization in the cell body (Fig. 8 D). We found that Rab5[DN] and Rab5[CA] dramatically affected dSNX16-decorated endosome structures. dSNX16 localized to exaggerated elongated threads in Rab5[CA]-expressing animals, consistent with more tubulated structures observed in dSNX16[3A]-expressing animals, while in Rab5[DN]-expressing animals, fewer tubulated dSNX16 endosomes were observed, similar to dSNX16[ΔCC]. We then asked if Rab5[CA]-induced endosome tubulation depended on the CC domain of SNX16. Indeed, we found that Rab5[CA] was able to tubulate endosomes in animals expressing dSNX16 or dSNX16[3A] as their only source of SNX16, but not in animals expressing dSNX16[ΔCC] (Fig. 8 E), providing strong evidence that this tubulation effect occurs specifically via the CC domain of SNX16. Notably, endosomes were still enlarged, suggesting that Rab5[CA] can still activate other effectors in the absence of the SNX16 CC domain.

Finally, we tested whether Rab7 similarly affected SNX16 endosome association and distribution. We found that dSNX16 was strongly concentrated at the NMJ in Rab7[CA]-expressing animals, consistent with previous findings (Akbergenova and Littleton, 2017), and was also largely depleted from the cell body (Fig. 8, A and B). By contrast, dSNX16 was slightly enriched at the cell body in Rab7[DN]-expressing animals. Thus, Rab7 manipulations shifted the distribution of dSNX16 between the NMJ and the cell body in the opposite direction of Rab5 manipulations but did not affect dSNX16 endosome association, suggesting that Rab7-dependent endosome distribution effects occur downstream of SNX16 endosome association.

Discussion

Here, we propose a working model for SNX16 in regulating neuronal growth factor signaling by controlling endosomal tubulation and distribution (Fig. 9). At the molecular level, SNX16, via its CC domain, oligomerizes into higher-order assemblies that promote tubulation of PI(3)P-containing membranes. At the cellular level, the SNX16 CC domain is required for its endosomal localization in both mammalian cells and *Drosophila* motor neurons. In these neurons, activation of Rab5 and CC-dependent self-association of SNX16 promote accumulation of SNX16 endosomes in Rab5- and Rab7-positive tubulated compartments in the cell body and regulate the localization and activity of the synaptic growth-promoting BMP receptor Tkv. Our results suggest that higher-order assembly of SNX16 on endosomes can control compartment identity and distribution to regulate the signaling activities of receptors in neurons.
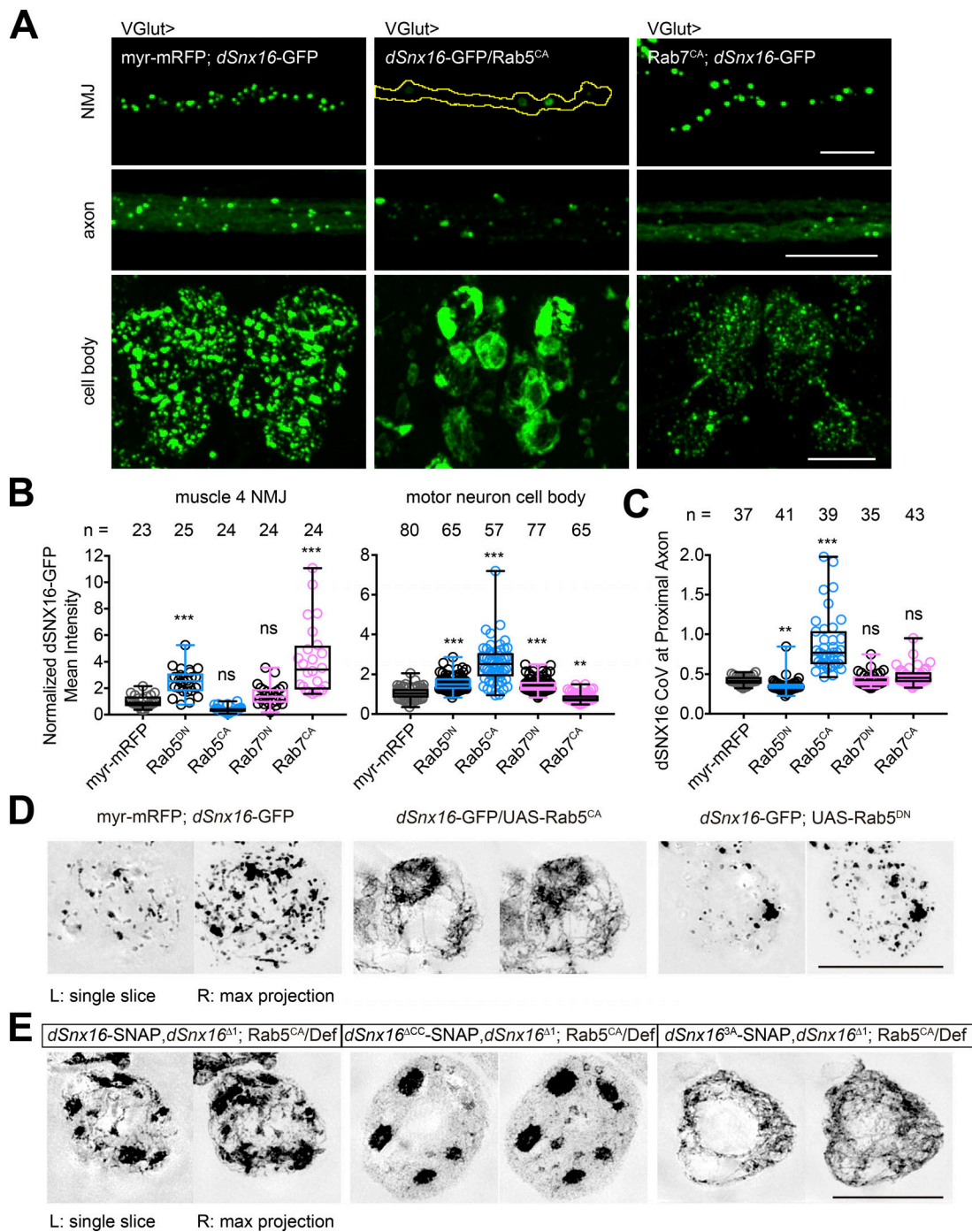
Figure 8. **Manipulations of endosomal trafficking alter wild type dSNX16 endosome structure, localization and distribution in the neuron.** **(A)** Representative images of animals expressing VGlut-GAL4-driven UAS-*dSnx16*-GFP together with Rab5[CA], or Rab7[CA] at the NMJ, the proximal axon, and the cell body. myr-mRFP serves as a UAS control. **(B)** dSNX16-GFP mean intensity quantification at the NMJ and the cell body. **(C)** CoV of dSNX16-GFP at proximal axon. **(D)** Representative SIM images of animals expressing VGlut-GAL4-driven UAS-*dSnx16*-GFP together with Rab5[DN] or Rab5[CA] at the cell body. L, left panel; R, right panel. **(E)** Representative SIM images of animals expressing VGlut-GAL4–driven UAS-*dSnx16*-SNAP variants together with Rab5[CA] in the *dSnx16* null background. Quantification is from ≥23 NMJs, 35 axons, or 57 cell bodies analyzed using a Kruskal–Wallis test followed by Dunn's multiple comparisons test. Intensity measurements were normalized to mean intensity in the wild-type dSNX16 condition. All images show 2D maximum intensity projections of confocal stacks unless noted otherwise. Data are shown as box-and-whisker plots with all data points superimposed. **, $p < 0.01$; ***, $p < 0.001$. ns, not significant. Scale bars, 10 µm.

Membrane tubulation activity of SNX16

SNX16 is selectively localized to dynamic tubular late-endosome structures in vivo (Brankatschk et al., 2011), but its function on these structures has been unclear. Here, we provide direct evidence that SNX16 can generate membrane tubules via CC domain–mediated higher-order assembly (Fig. 3). Interestingly,
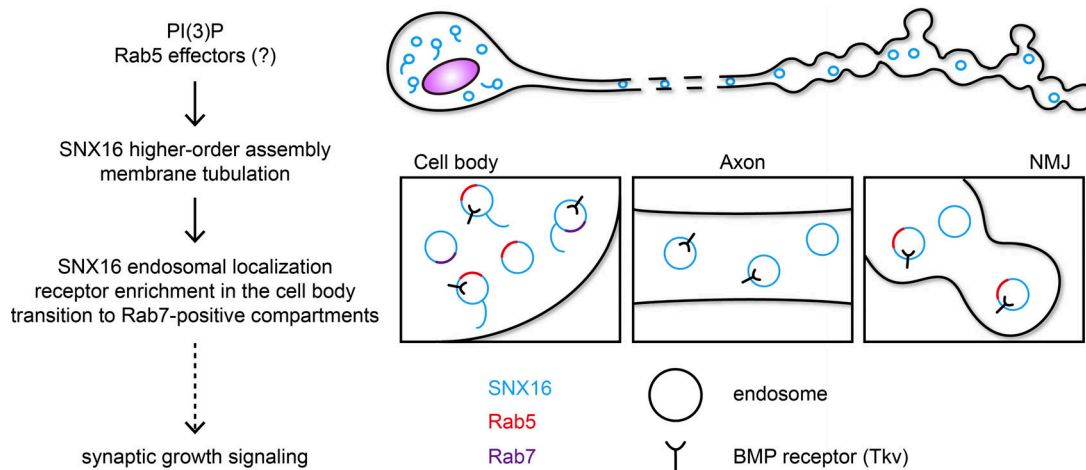
Figure 9. **Working model for SNX16 function.** The SNX16 CC domain controls its higher-order assembly and membrane tubulation capabilities. In *Drosophila* motor neurons, SNX16 oligomerization promotes its endosome association and redistribution from Rab5-positive endosomes at the NMJ to tubulated Rab5- and Rab7-positive endosomes in the cell body containing the BMP receptor Tkv. SNX16 oligomerization may be regulated by Rab GTPases and/or PI(3)P levels in vivo.

SNX16 does not contain predicted membrane remodeling domains such as the amphipathic helices or BAR domains found in the SNX-BAR subfamily (Pylypenko et al., 2007; van Weering et al., 2012) and therefore may deform membranes by one of several potential (and nonexclusive) mechanisms (McMahon and Gallop, 2005; McMahon and Boucrot, 2015). First, higher-order assemblies of SNX16 may form a scaffold that imposes membrane curvature, as has been proposed for oligomers composed of Retromer and the PX-only protein SNX3 (Lucas et al., 2016). This model is supported by our cross-linking results and the reduced FRAP recovery we observe for SNX16 under conditions in which tubules form (Fig. 2), as well as previous results indicating multivalent self-association of SNX16 via the PX and CC domains (Choi et al., 2004b). High-resolution EM studies of SNX16-decorated tubules will be required to resolve the oligomeric state and organization of these SNX16 assemblies. Second, the predicted unstructured regions in the N- and C-termini of SNX16 (Fig. 1 A) may facilitate the scaffolding-induced membrane tubulation via protein crowding (Stachowiak et al., 2010, 2012; Zeno et al., 2018). Third, the hSNX16 structure indicates that the hydrophobic residue F220, which is required for membrane binding, is positioned to penetrate into the membrane (Xu et al., 2017), potentially leading to wedging-induced membrane curvature. Indeed, our observation that higher-order assemblies of SNX16 are salt insensitive for membrane binding suggest that these interactions may be mediated by such hydrophobic interactions (Fig. 1, E and F). Further biophysical studies of SNX16 membrane insertion will be required to test these hypotheses.

Role of dSNX16 in endosome distribution

In addition to regulating the structure of neuronal endosomes, we made the unexpected finding that self-association promotes SNX16 redistribution from Rab5-positive endosomes at the axon terminal to Rab5- and Rab7-positive endosomes in the cell body. One possibility is that SNX16-positive structures

are independently generated in the cell body and at the NMJ, similar to local recycling of Trk receptors (Ascaño et al., 2009). Alternatively, SNX16 endosomes may play a role in long-range transport of cargo from the NMJ to the cell body. In favor of this model, mammalian SNX16 copurifies with retrogradely transporting, maturing compartments in neurons (Debaisieux et al., 2016). Further, we observed occasional retrograde cotransport of dSNX16 and Tkv particles (Fig. 6 E and Videos 1 and 2), suggesting that SNX16 endosomes may play an active role in Tkv retrograde transport. Indeed, exit of Rab7-positive endosomes from the NMJ promotes BMP signaling (Liao et al., 2018), similar to TrkA receptor retrograde transport (Ye et al., 2018). However, many axonal dSNX16 particles are stationary, and many motile Tkv particles do not contain dSNX16, so while it is possible that a small number of transport carriers are sufficient to mediate Tkv redistribution, we cannot exclude the existence of additional, SNX16-independent transport carriers for both active and inactive Tkv. Taken together, our findings suggest that the endosome maturation/tubulation that occurs with SNX16 self-association is coupled with enhanced retrograde transport.

Role of dSNX16 tubules in vivo

Consistent with its in vitro tubulation capability (Fig. 3) and the tubular localization of hSNX16 in HeLa cells (Brankatschk et al., 2011), we observed wild-type dSNX16 on tubular structures that exclude the Tkv receptor at *Drosophila* motor neuron cell bodies (Fig. 6 H). The exclusion of Tkv from SNX16-decorated tubules stands in contrast to SNX-PX-BAR–decorated tubules, which colocalize with and sort cargo directly (Cullen and Steinberg, 2018), suggesting that different SNXs may either promote or restrict cargo transport in the endosomal pathway. The tubule localization of SNX16 is CC domain dependent, and we observed increased numbers of tubular compartments in our hyper-oligomerized SNX16[3A] mutant (Fig. 5 B). This mutant also promotes BMP receptor accumulation in endosomes (Fig. 6) as well

as transcription of BMP target genes such as *trio* (Rodal et al., 2011). Taken together, our results raise the intriguing possibility that SNX16 tubules promote signaling by antagonizing BMP receptor down-regulation, perhaps by removing other cargoes that would otherwise promote endosome maturation or lysosome fusion. Consistent with this hypothesis, overexpression of SNX16 blocks escape of viral RNA from multivesicular bodies (Le Blanc et al., 2005). Further, multivesicular bodies accumulate at SNX16[3A]-expressing NMJs (Rodal et al., 2011), and SNX16 is found on intermediate Rab7- and LAMP1-positive, but not later LBPA- or CD63-positive, endosomes (Brankatschk et al., 2011), suggesting that it may prevent endosome maturation.

Somewhat surprisingly, our dSNX16[ΔCC] mutant also promoted BMP-dependent synaptic growth (Fig. 6, A–C), despite exhibiting reduced endosomal localization and endosome tubulation in the cell body (Fig. 5). This suggests a more complex and interesting model than the simple idea that tubulation alone promotes endosomal BMP signaling and that dSNX16[ΔCC] should behave like a loss-of-function mutant. Despite being expressed at lower levels, we found that dSNX16[ΔCC] colocalized as well as wild-type dSNX16 to Tkv-positive endosomes in the cell body and axon (Fig. 6) and increased the distribution of FYVE from the cytosol to endosomes (Fig. S4 F). This suggests that Tkv is enriched in SNX16[ΔCC]-positive PI(3)P-rich endosomes. Interestingly, similarly PI(3)P-rich endosomes suppress EGFR inactivation in nonneuronal cell lines (Cao et al., 2008) and dynein-mediated axonal transport in hippocampal neurons (Lorenzo et al., 2014), indicating that they may be permissive for signaling.

Synthesizing these results, we hypothesize that SNX16[ΔCC] endosomes represent a block at an early, highly signal-permissive state that can nonetheless still target cargo for degradation, resulting in net lower levels of Tkv, Rab5, and Rab7 in the cell body. SNX16[3A] endosomes on the other hand may represent a more mature blocked state in which endosomes accumulate in the cell body and protect Tkv from degradation. Our data overall suggest that the CC domain is required to attenuate signaling at endosomes (perhaps by preventing endosome maturation or sequestering Tkv from cytoplasmic signaling), while an overactive CC blocks progression of Tkv to degradation.

In vivo regulation of dSNX16 oligomerization

dSnx16[3A] and *dSnx16* null mutants exhibit opposite synaptic growth phenotypes (Rodal et al., 2011), and dSNX16[3A] potentiates the normal in vitro activities of SNX16, suggesting that it functions as a dominant-active mutant and that in vivo mechanisms of wild-type SNX16 regulation might similarly promote its oligomerization and endosome tubulation activities. Manipulation of Rab5 and Rab7 has previously been shown to affect dSNX16 levels at the NMJ (Akbergenova and Littleton, 2017), suggesting that these endosome regulators may control SNX16 activity. We found that GTP-locked Rab5[CA] promotes endosome association, CC-dependent tubulation, and redistribution of wild-type dSNX16 from the NMJ to the cell body (identically to dSNX16[3A]), while GDP-locked Rab5[DN] produces the opposite phenotypes, suggesting that dSNX16

oligomerization and endosome tubulation may be regulated by Rab5 (Fig. 8). This may occur via direct effects on SNX16 CC interactions via an as-yet-unknown Rab5 effector. Alternatively, Rab5 may regulate SNX16 activity by increasing PI(3)P levels (Shin et al., 2005), which can promote SNX16 membrane binding and remodeling in vitro. Separating these mechanisms will require developing tools to distinguish SNX16 CC-mediated oligomerization from PI(3)P binding. By contrast, manipulation of Rab7 did not directly phenocopy the effects of SNX16 oligomerization and instead primarily resulted in the redistribution of SNX16 between the cell body and NMJ. Thus, Rab7 regulates transport of SNX16 endosomes, but not assembly of SNX16 on these endosomes. Our previous results indicating that SNX16 acts downstream of the membrane-remodeling F-BAR/SH3 protein Nwk, which constrains synaptic growth signaling (Rodal et al., 2011), suggest that Nwk acts antagonistically to the Rab5 pathway to limit SNX16 activity. Further studies will be required to determine where Nwk and other potential SNX16-interacting factors act in this pathway and integrate opposing SNX16 regulatory mechanisms that control endosome maturation and distribution (Fig. 9).

Materials and methods

Plasmid construction

Full-length hSNX16 was cloned into pcDNA3.1 using Gateway technology (Invitrogen) from Addgene plasmid 23617. hSNX16 variants were generated in this construct by site-directed mutagenesis. hSNX16[3A] (E231A, E234A, and E235A) was generated with the following primer set: forward, 5′-CCTAGAAGAAAG CAGGGCATTCTGTGCGACTTTAGCCGCGACAAACTACCGCTT ACAGAAAGAAC-3′; and reverse, 5′-GTTCTTTCTGTAAGCGGT AGTTTGTCGCGGCTAAAGTCGCACAGAATGCCCTGCTTTCTT CTAGG-3′. hSNX16[ΔCC] (aa 230–278 deletion) was generated with the following primer set: forward, 5′-GCCTAGAAGAAAGCAGGG CATTCCCTGAAGAATCACTGGATGTG-3′; and reverse, 5′-CAC ATCCAGTGATTCTTCAGGGAATGCCCTGCTTTCTTCTAGGC-3′. hSNX16[Y145A] was generated with the following primer set: forward, 5′-CCCCAGAAGAAAGCTGGGTAGTTTTCAGAAGAGCTA CTGACTTCTCTAGGCTTAATGAC-3′; and reverse, 5′-GTCATT AAGCCTAGAGAAGTCAGTAGCTCTTCTGAAAACTACCCAGCT TTCTTCTGGGG-3′. For expression in rat hippocampal neurons, hSNX16 and mutants were amplified via PCR (with the primer set forward, 5′-GCGCGGAATTCCCATGGCAACTCCTTATGTCCC-3′; and reverse, 5′-GCGCGCTCGAGCTAGTCTTCTTCAGCATCA TATGCCA-3′) and cloned into pCMV-myc. For expression and purification of hSNX16 variants, wild-type and mutant hSNX16 were amplified via PCR and cloned into pGEX-6P (GE Healthcare; with the following primer set: forward, 5′-GCGCGGAATTCCATG GCAACTCCTTATGTCCC-3′; and reverse, 5′-GCGCGCTCGAGC TAGTCTTCTTCAGCATCATATGCCA-3′) and into pTrcHis-Xpress-SNAP vectors (Kelley et al., 2015; with the following primer set: forward, 5′-GCGCGGGATCCCATGGCAACTCCTTATGTCCC-3′; and reverse, 5′-GCGCGGGCGCGCCCACCCTTGTCTTCTTCAGCATCA TATGCCA-3′). All constructs were verified by sequencing. pGEX-4T-hSNX1 was a gift from P. Cullen (Indiana University, Bloomington, IN).

Protein purification

BL21 DE3 cells transformed with the indicated constructs were grown to log phase and induced with 0.4 M IPTG at 18°C for 12 h. GST fusion proteins and His-Xpress-SNAP–tagged proteins were purified as previously described (Becalska et al., 2013; Kelley et al., 2015).

GST fusion proteins were purified from *Escherichia coli* extracts on glutathione agarose resins (Thermo Fisher Scientific), followed by PreScission protease (GE Healthcare) cleavage at 4°C for 16 h. Released SNX16 variants were then gel filtrated through a Superdex 75 column in 20 mM Tris, 50 mM KCl, 0.1 mM EDTA, and 0.5 mM DTT, pH 7.5. Peak fractions were determined from SDS-PAGE analysis, concentrated, aliquoted, flash frozen in liquid N_2, and stored at −80°C. For BS^3 cross-linking assays, proteins were gel filtered in 20 mM Hepes buffer instead of 20 mM Tris buffer.

His-Xpress-SNAP–tagged proteins were purified from *E. coli* extracts on nickel-nitrilotriacetic acid agarose beads (Qiagen), followed by gel filtration on a Superose 12 column (GE Healthcare) in 20 mM Tris, 50 mM KCl, 0.1 mM EDTA, and 0.5 mM DTT, pH 7.5. The concentrated peak fractions were supplemented with 1 mM DTT and incubated at 25°C for 2 h with a 5-M excess of SNAP-Surface Alexa Fluor 488 (New England Biolabs). The final protein product was exchanged into 20 mM Tris, 50 mM KCl, 0.1 mM EDTA, and 0.5 mM DTT, pH 7.5, using a PD-10 desalting column (GE Healthcare), aliquoted, flash frozen in liquid N_2, and stored at −80°C.

In vitro liposome cosedimentation and BS^3 cross-linking assays

Lipid cosedimentation assays were conducted as previously described (Becalska et al., 2013). DOPS, PI(3)P, and rhodamine PE were obtained from Avanti Polar Lipids; DOPC and DOPE were obtained from Echelon Biosciences. To generate liposomes, lipids were mixed in the indicated ratios and dried under a stream of argon gas, followed by 1 h under vacuum. Lipid films were then hydrated in 20 mM Hepes, pH 7.5, and 100 mM NaCl for 2 h at 37°C to a final concentration of 1.5 mM.

In the cosedimentation assays (all performed in triplicate), 10 µl of 1.5 mM liposomes (0.5 mM final concentration) with the indicated PI(3)P composition (0.05%, 1%, 2.5%, 5%, and 10%) was incubated with 20 µl of 3 µM protein (2 µM final concentration, in 20 mM Hepes, pH 7.5, and 100 mM NaCl) for 30 min at room temperature, followed by centrifugation at 18,000 ×g for 20 min at 4°C. For salt sensitivity experiments, proteins and liposomes were incubated in 100 mM NaCl or 400 mM NaCl for 45 min or 100 mM NaCl for the first 30 min then in 400 mM NaCl for the following 15 min. Proteins were prespun under the same conditions before incubation with lipids. To measure membrane-bound fraction, pellets and supernatants were separated and equal amounts were fractionated by SDS-PAGE, stained with Coomassie, and quantified by densitometry on a LI-COR Odyssey instrument. Membrane-bound hSNX16 fraction was quantified as hSNX16 intensity in the pellet/(hSNX16 intensity in the pellet + hSNX16 intensity in the supernatant).

For BS^3 cross-linking assays, 10 µl of 1.5 mM 1% PI(3)P liposomes (0.5 mM final concentration) was incubated with 20 µl of 7.5 µM protein (5 µM final concentration) for 30 min at room temperature with BS^3 (Thermo Fisher Scientific) at the indicated concentrations (125 nM, 2.5 µM, 5 µM, 12.5 µM, and 25 µM in the liposome cosedimentation assay; 25 nM, 50 nM, 125 nM, 2.5 µM, 5 µM, 12.5 µM, and 25 µM in the Hepes buffer alone assay). 1 µl of 1 M Tris was added to each reaction to stop cross-linking for 15 min at room temperature. Samples were then centrifuged, run on 7.5% SDS-PAGE gel, and imaged on a LI-COR Odyssey instrument as described in cosedimentation assays.

To account for the fact that hSNX16 pellet fraction and supernatant fraction were run on different gels in the BS^3 cross-linking assays, membrane-bound hSNX16 variants were quantified from the pellet and supernatant gels individually. In the pellet-fraction gels, hSNX16 intensity measured in the no-BS^3 condition was considered the liposome-bound protein intensity. Intensity measurements were normalized to wild-type hSNX16 intensity. In the supernatant-fraction gels, intensity measured in 0% PI(3)P liposome supernatant was considered the total protein intensity; intensity measured in the no-BS^3 condition was considered the unbound protein intensity. The membrane-bound hSNX16 fraction was quantified as (total protein intensity – unbound protein intensity)/ total protein intensity. To control for background, pellet-fraction gels or supernatant-fraction gels of hSNX16 variants were stained in the same container and scanned in one image.

In vitro GUV assays and FRAP analysis

GUVs were generated by electroformation in a Vesicle Prep Pro device (Nanion Technologies) or through gentle hydration in 5 mM Hepes and 300 mM sucrose, pH 7.5, as described previously (Kelley et al., 2015). Approximately 30 µM GUVs (300 nM PI(3)P was mixed with 100 nM or 500 nM SNAP-tagged proteins in 10 mM Hepes and 150 mM KCl, pH7.5; incubated for 45 min; and imaged in µ-Slide Angiogenesis devices (ibidi). All GUV stacks were acquired at 0.5-µm steps using SlideBook software (3I) on a Marianas spinning-disk confocal system (3I), which consists of an Observer Z1 microscope (Carl Zeiss) equipped with a CSU-X1 spinning-disk confocal head (Yokogawa) and a QuantEM 512SC EM charge-coupled device (CCD) camera (Photometrics) with a 100× (NA 1.45) oil-immersion objective at room temperature. Stack images were exported as tiffs into FIJI (National Institutes of Health) for quantification.

To quantify the percentage of tubulated GUVs, the lipid channel (rhodamine PE) was used to identify unilamellar vesicles. The protein channel (SNAP 488) was then used to count tubules for each GUV. The number of tubules reflected tubules observed in the whole Z stack.

For FRAP experiments, 1% agarose in 10 mM Hepes and 150 mM KCl, pH 7.5, was added to limit GUV mobility (0.33% final agarose percentage). GUVs were imaged for 6 min at 2-s intervals, with a pause for bleaching after time point 10 (the 20th second, shown as time point 0 in graphs). Signal intensity over time from a nonbleached region of the same GUV was used to correct for photobleaching. Protein fluorescence was further normalized by subtracting the intensity at bleaching (time point 10) from all time points and divided by prebleach intensity. Because lipid fluorescence recovered before the first time point

was recorded (time point 10), it was not normalized and was only corrected for photobleaching.

Negative staining and EM
Liposomes for negative staining were generated at 1.5 mM as described in liposome cosedimentation assays with 10% PI(3)P and extruded through a 200-nm filter (Avanti Polar Lipids). Liposomes (0.5 mM) were incubated with protein for 30 min. Samples were applied to copper grids coated with continuous carbon, negatively stained with 2% uranyl acetate (JT Baker Chemical), and imaged using a Morgagni 268 transmission electron microscope (FEI) operating at 80 kV and equipped with a 1,000 × 1,000 CCD camera (Gatan).

Mammalian cell culture, transfection, immunostaining, and imaging
Dissociated rat hippocampal neurons were cultured on a feeder layer of astrocytes as previously described (Herzog et al., 2017). Briefly, a layer of confluent astrocytes was generated by plating the cells onto 12-mm glass coverslips coated with poly-D-lysine (20 µg/ml) and laminin (3.4 µg/ml) in 24-well plates. Dissociated hippocampi from embryonic dat 18 rat embryos were plated on this layer of astrocytes at a density of 80,000 cells per well and grown in Neurobasal medium supplemented with B27 (Thermo Fisher Scientific) at 37°C. Neurons were transfected at day in vitro (DIV) 2 using the calcium phosphate transfection method (Xia et al., 1996) at 500 ng/well per plasmid and fixed on DIV 7 with 4% PFA + 4% sucrose solution in PBS. The pCMV-GFP plasmid was cotransfected with myc-hSNX16 variants to visualize individual neurons. Fixed neurons were then incubated with mouse anti-Myc antibody (9e10 1:500; A5963; Sigma) diluted in gelatin blocking buffer at 4°C overnight in a humidified chamber, followed by 2-h secondary antibody incubation at room temperature. Coverslips were then washed and mounted on glass microscope slides with Aquamount (Lerner Laboratories).

Human adenocarcinoma HeLa and MCF7 cells and human osteosarcoma U2OS cells (ATCC) were grown in standard DMEM (GIBCO BRL Life Technologies) supplemented with 2 mM L-glutamine (Thermo Fisher Scientific) and 10% FBS at 37°C with 5% CO_2. Cells were seeded on collagen I-coated (50 µg/ml, Advanced BioMatrix) 12-mm glass coverslips in 24-well plates before transfection. HeLa cells and U2OS cells were transfected at 40–50% confluence using polyethylenimine (Polysciences) as previously described (Jansen et al., 2015). MCF7 cells were transfected at 70% confluence using Lipofectamine 3000 (Thermo Fisher Scientific) according to the manufacturer's instructions. Cells were fixed in 4% PFA in PBS 24 h after transfection. Fixed U2OS cells were incubated with mouse anti-EEA1 antibody (clone 14 1:1,000; 610457; BD Biosciences) for 1 h in a humidified chamber, followed by 1-h secondary antibody incubation at room temperature. Coverslips were washed and mounted on glass microscope slides with Aquamount (Lerner Laboratories).

HeLa cells were imaged on a Marianas spinning-disk confocal system (as described above for GUVs). All other cell types were imaged at room temperature on an Andor spinning-disk confocal system, which consists of a Nikon Ni-E upright microscope equipped with a Yokogawa CSU-W1 spinning-disk head and an Andor iXon 897U EMCCD camera. HeLa, U2OS, and MCF7 cells were acquired in NIS Elements AR software (Nikon) with a 100× (NA 1.45) oil-immersion objective at 0.2-µm steps. Cultured rat hippocampal neurons were acquired with a 60× (NA 1.4) oil-immersion objective at 0.3-µm steps. Images for each independent experiment were acquired and shown with identical settings for all conditions. To quantify CoV of myc-hSNX16 intensity in the hippocampal neuron cell bodies, sum projections were generated from individual Z stacks with FIJI (Schindelin et al., 2012). Cell bodies were manually outlined in the GFP channel for transfected neurons. The mean fluorescence intensity and intensity standard deviation of myc-hSNX16 variants were then measured in that area to calculate CoV (standard deviation/mean fluorescence intensity). To quantify hSNX16 and hSNX16[3A] pixel intensity distributions in single-slice HeLa cells, cells were manually outlined. Images were normalized to the mean hSNX16 intensity in this area, and pixel intensity distributions were calculated using the Sixteen Bit Histogram plugin in ImageJ. Data were binned as indicated and graphed using Prism software (GraphPad).

Drosophila stocks, culture, and imaging
Flies were cultured using standard media and techniques. UAS-dSnx16-SNAP plasmids were constructed into pUAST-AttB (Brand and Perrimon, 1993) via Gibson assembly from previously generated UAS-dSnx16-GFP plasmids (Rodal et al., 2011) using the following primers: forward, 5′-GAATTCGTTAACAGATCTGCGGCCGCCCCCTTCACCAT-3′; reverse, 5′-TGGTGCGCTTGCATGCGATATCAACCACTTTGTACAAGAAAGC-3′; forward, 5′-TATCGCATGCAAGCGCACCACCCTGGAT-3′; and reverse, 5′-TAGAGGTACCCTCGAGCCGCTTAATGGGATCCTGGCGCG-3′). dSNX16[ΔCC] (aa 345–393 deletion) was generated by site-directed mutagenesis with the following primer set: forward, 5′-CCATGGAGGAGTGTCGTGCAATTTGCTCGCACTGCTCCTCAGCTAGCG-3′; and reverse, 5′-CGCTAGCTGAGGAGCAGTGCGAGCAAATTGCACGACACTCCTCCATGG-3′. Sequence-verified constructs were injected into w1118 flies at AttP40 (Markstein et al., 2008) at Rainbow Transgenic Flies. Previously described fly stocks include VGlut-GAL4 (X; Daniels et al., 2008), Snx16[Δ1], Df(2R) Exel7150, UAS-dSnx16-GFP, UAS-dSnx16[3A]-GFP (Rodal et al., 2011), UAS-Tkv-mCherry (Deshpande et al., 2016), GFP-Rab5[KI] (Fabrowski et al., 2013), YFP-myc-Rab7[KI] (Dunst et al., 2015), UAS-Rab7[DN] (Rab7[T22N]; Assaker et al., 2010), UAS-Rab11[DN] (Rab11[N124I]; Satoh et al., 2005), UAS-Rab11[CA] (Rab11[Q70L]; Emery et al., 2005), UAS-hTfR (Strigini and Cohen, 2000), and UAS-Tkv[Q199D] (Hoodless et al., 1996). Larvae overexpressing a Rab5[CA] in motor neurons exhibit grossly normal crawling behavior and eclose as adults at normal rates, while larvae overexpressing Rab7[CA] crawl more slowly and eclose at lower rates. The following stocks were obtained from the Bloomington Drosophila Stock Center (stock number indicated in parentheses): UAS-myr-mRFP (BL7118), UAS-Rab5[DN] (Rab5[S43N]; BL42703), UAS-Rab5[CA] (Rab5[Q88L]; BL43335), UAS-Rab7[CA] (Rab7[Q67L]; BL42707), UAS-Myc-2xFYVE-GFP (BL42712), wit[A12] (BL5173), and wit[B11] (BL5174).

For protein localization in *Drosophila*, flies were cultured at controlled density at 25°C. Wandering third-instar larvae (a minimum of six per genotype) were dissected in calcium-free HL3.1 saline (Feng et al., 2004) and then fixed in HL3.1 (or PBS for pMad staining) containing 4% formaldehyde for 15 min. Fillets were then stained with mouse α-Rab11 (clone 47, 1:100, 4°C overnight; 610656; BD Biosciences), mouse α-hTfR (1:2,000, 2 h at room temperature; 236-15375; Invitrogen), mouse α-Synapsin (1:1,000, 4°C overnight; 3C11; Developmental Studies Hybridoma Bank), or rabbit α-pMad (Persson et al., 1998; 1:1,000, 4°C overnight). Larvae expressing dSNX16-SNAP variants were stained for 15 min with 2 µM SNAP-Surface 488 (New England Biolabs) or for 2 min with 0.5 µM JF549-cpSNAP-tag ligand, both diluted in PBS (Luke Laevis, Janelia Research Campus, Ashburn, VA; Kohl et al., 2014), followed by 1 h of goat α-HRP 647 staining (1:250; 123-605-021; Jackson ImmunoResearch Laboratories) at room temperature. For subcellular and colocalization analysis, type 1b NMJs from segment A2 and A3 on muscle 4 were imaged at room temperature on a Nikon Ni-E upright spinning disk confocal microscope as described above using a 60× NA 1.4 or 100× NA 1.45 oil-immersion objective; two fields of proximal axons were imaged within 100 µm of the ventral ganglio, and four sets of MNISN-I cell bodies were imaged from the posterior end of the ventral ganglion (Choi et al., 2004a). Images for each independent experiment were acquired with identical settings for all genotypes and are shown at identical contrast except where indicated. Single NMJ stack images, single axon stack images, and single-slice cell body images were manually cropped for intensity quantification. For analysis of NMJ morphology, type 1b NMJs from segment A2 and A3 on muscle 4 were imaged. α-Synapsin was used for manual bouton counting in ImageJ, from 2D projections of confocal stacks. Only type Ib innervation was quantified.

Mean fluorescence intensity and CoV were performed on background-intensity–subtracted sum intensity projections at the NMJ and proximal axons and on single slices at the cell body, with the exception that CoV was quantified on maximum intensity projection at the proximal axon in Fig. 5 C because of the strong cytoplasmic localization. The PCC was calculated using Coloc2 (FIJI) on maximum intensity projections at the NMJ and proximal axons and on single slices at the cell body. For pMad levels at the ventral ganglion, mean pMad intensities were measured within a single, central slice of dSNX16-positive cell bodies.

For live imaging, wandering third-instar larvae were dissected in room temperature HL3.1, leaving the central nervous system and axons intact. Dissected larvae were then transferred onto a glass slide for imaging in a drop of HL3.1, and a coverslip was affixed to the glass slide by double-sided tape (3M). Segmental nerve bundles were imaged ~100 µm from the ventral ganglion at 1.5 s per Z stack. Larvae were imaged for a maximum of 30 min after dissection. All samples were imaged at room temperature using a Nikon Ni-E upright spinning disk confocal microscope as above, enabled for simultaneous two-color acquisition with a TuCam device (GFP-mCherry 532/617 mirror; Andor) and two iXon 897U EMCCD cameras. For axonal transport quantification, videos were registered using FIJI MultiStackReg when necessary, and a kymograph was generated using the FIJI KymographBuilder by drawing a straight line from the proximal to the distal end of the in-focus region of the axon bundle. Retrograde, anterograde, and stalled particles were manually counted from the SNX16-GFP channel and then correlated with Tkv signal.

For SIM, images in the cell body were collected at room temperature at 0.2-µm steps on a Nikon N-SIM instrument equipped with an Apo total internal reflection fluorescence 100× (NA 1.4) oil-immersion objective. Images were acquired using a violet-to-red diffraction grating at three angles and five phases of illumination, producing 15 raw images for SIM analysis, and reconstructed with default stack reconstruction setting in NIS Elements software. SIM images were not acquired at identical settings due to the sensitivity of SIM reconstruction to signal intensity.

Statistical analyses

All errors shown are mean ± SEM in xy and column graphs, as well as for quantifications reported in the text. All box-and-whisker plots are superimposed with individual data points. The box extends from the 25th to 75th percentiles with the median in the middle, and the whiskers mark the lowest data point to the highest. Data were tested for normality using a D'Agostino–Pearson omnibus normality test, and statistical significance was calculated using a one-way ANOVA followed by Tukey's test, Kruskal–Wallis tests followed by multiple Dunn comparisons, or a Mann–Whitney U test in Prism software (GraphPad) as indicated in the figure legends (*, $P < 0.05$; **, $P < 0.01$; ***, $P < 0.001$). Comparisons are to the leftmost genotype in each bar graph, unless indicated otherwise by horizontal bars.

Online supplemental material

Fig. S1 shows quantification of liposome binding of hSNX16 CC variants, cross-linking of hSNX16 CC variants without liposomes, and representative time-lapse images and FRAP quantification. Fig. S2 shows a schematic of the NMJ, proximal axon, and cell body and representative images and quantification of dSNX16 levels in dSNX16-GFP and dSNX16[3A]-GFP lines. Fig. S3 shows representative images and quantification of Tkv-mCherry levels and localization in dSNX16-GFP and dSNX16[3A]-GFP lines as well as representative images and the quantification of hTfR levels and localization in dSNX16-SNAP lines. Fig. S4 shows representative images and quantification of dSNX16 CC variant endosomal localization. Fig. S5 shows representative images and quantification of wild-type dSNX16 levels upon Rab manipulation. Videos 1 and 2 show retrogradely cotransported dSNX16-GFP and Tkv-mCherry particles along segmental axon bundles of *Drosophila* third-instar larvae.

Wang et al.
Regulation of neuronal membrane traffic by SNX16

Journal of Cell Biology 2616
https://doi.org/10.1083/jcb.201811074

References

Akbergenova, Y., and J.T. Littleton. 2017. Pathogenic Huntington Alters BMP Signaling and Synaptic Growth through Local Disruptions of Endosomal Compartments. *J. Neurosci.* 37:3425–3439. https://doi.org/10.1523/JNEUROSCI.2752-16.2017

Ascaño, M., A. Richmond, P. Borden, and R. Kuruvilla. 2009. Axonal targeting of Trk receptors via transcytosis regulates sensitivity to neurotrophin responses. *J. Neurosci.* 29:11674–11685. https://doi.org/10.1523/JNEUROSCI.1542-09.2009

Assaker, G., D. Ramel, S.K. Wculek, M. González-Gaitán, and G. Emery. 2010. Spatial restriction of receptor tyrosine kinase activity through a polarized endocytic cycle controls border cell migration. *Proc. Natl. Acad. Sci. USA.* 107:22558–22563. https://doi.org/10.1073/pnas.1010795108

Barford, K., C. Deppmann, and B. Winckler. 2017. The neurotrophin receptor signaling endosome: Where trafficking meets signaling. *Dev. Neurobiol.* 77:405–418. https://doi.org/10.1002/dneu.22427

Becalska, A.N., C.F. Kelley, C. Berciu, T.B. Stanishneva-Konovalova, X. Fu, S. Wang, O.S. Sokolova, D. Nicastro, and A.A. Rodal. 2013. Formation of membrane ridges and scallops by the F-BAR protein Nervous Wreck. *Mol. Biol. Cell.* 24:2406–2418. https://doi.org/10.1091/mbc.e13-05-0271

Brand, A.H., and N. Perrimon. 1993. Targeted gene expression as a means of altering cell fates and generating dominant phenotypes. *Development.* 118:401–415.

Brankatschk, B., V. Pons, R.G. Parton, and J. Gruenberg. 2011. Role of SNX16 in the dynamics of tubulo-cisternal membrane domains of late endosomes. *PLoS One.* 6:e21771. https://doi.org/10.1371/journal.pone.0021771

Cao, C., J.M. Backer, J. Laporte, E.J. Bedrick, and A. Wandinger-Ness. 2008. Sequential actions of myotubularin lipid phosphatases regulate endosomal PI(3)P and growth factor receptor trafficking. *Mol. Biol. Cell.* 19:3334–3346. https://doi.org/10.1091/mbc.e08-04-0367

Chandra, M., and B.M. Collins. 2018. The Phox Homology (PX) Domain. *Adv. Exp. Med. Biol.* https://doi.org/10.1007/5584_2018_185

Chandra, M., Y.K. Chin, C. Mas, J.R. Feathers, B. Paul, S. Datta, K.E. Chen, X. Jia, Z. Yang, S.J. Norwood, et al. 2019. Classification of the human phox homology (PX) domains based on their phosphoinositide binding specificities. *Nat. Commun.* 10:1528. https://doi.org/10.1038/s41467-019-09355-y

Choi, J.H., W.P. Hong, M.J. Kim, J.H. Kim, S.H. Ryu, and P.G. Suh. 2004b. Sorting nexin 16 regulates EGF receptor trafficking by phosphatidylinositol-3-phosphate interaction with the Phox domain. *J. Cell Sci.* 117:4209–4218. https://doi.org/10.1242/jcs.01233

Choi, J.C., D. Park, and L.C. Griffith. 2004a. Electrophysiological and morphological characterization of identified motor neurons in the Drosophila third instar larva central nervous system. *J. Neurophysiol.* 91:2353–2365. https://doi.org/10.1152/jn.01115.2003

Cullen, P.J. 2008. Endosomal sorting and signalling: an emerging role for sorting nexins. *Nat. Rev. Mol. Cell Biol.* 9:574–582. https://doi.org/10.1038/nrm2427

Cullen, P.J., and F. Steinberg. 2018. To degrade or not to degrade: mechanisms and significance of endocytic recycling. *Nat. Rev. Mol. Cell Biol.* 19:679–696. https://doi.org/10.1038/s41580-018-0053-7

Daniels, R.W., M.V. Gelfand, C.A. Collins, and A. DiAntonio. 2008. Visualizing glutamatergic cell bodies and synapses in Drosophila larval and adult CNS. *J. Comp. Neurol.* 508:131–152. https://doi.org/10.1002/cne.21670

Debaisieux, S., V. Encheva, P. Chakravarty, A.P. Snijders, and G. Schiavo. 2016. Analysis of Signaling Endosome Composition and Dynamics Using SILAC in Embryonic Stem Cell-Derived Neurons. *Mol. Cell. Proteomics.* 15:542–557. https://doi.org/10.1074/mcp.M115.051649

Deshpande, M., and A.A. Rodal. 2016. The Crossroads of Synaptic Growth Signaling, Membrane Traffic and Neurological Disease: Insights from Drosophila. *Traffic.* 17:87–101. https://doi.org/10.1111/tra.12345

Deshpande, M., Z. Feiger, A.K. Shilton, C.C. Luo, E. Silverman, and A.A. Rodal. 2016. Role of BMP receptor traffic in synaptic growth defects in an ALS model. *Mol. Biol. Cell.* 27:2898–2910. https://doi.org/10.1091/mbc.E16-07-0519

Dunst, S., T. Kazimiers, F. von Zadow, H. Jambor, A. Sagner, B. Brankatschk, A. Mahmoud, S. Spannl, P. Tomancak, S. Eaton, and M. Brankatschk. 2015. Endogenously tagged rab proteins: a resource to study membrane trafficking in Drosophila. *Dev. Cell.* 33:351–365. https://doi.org/10.1016/j.devcel.2015.03.022

Emery, G., A. Hutterer, D. Berdnik, B. Mayer, F. Wirtz-Peitz, M.G. Gaitan, and J.A. Knoblich. 2005. Asymmetric Rab 11 endosomes regulate delta recycling and specify cell fate in the Drosophila nervous system. *Cell.* 122:763–773. https://doi.org/10.1016/j.cell.2005.08.017

Fabrowski, P., A.S. Necakov, S. Mumbauer, E. Loeser, A. Reversi, S. Streichan, J.A. Briggs, and S. De Renzis. 2013. Tubular endocytosis drives remodelling of the apical surface during epithelial morphogenesis in Drosophila. *Nat. Commun.* 4:2244. https://doi.org/10.1038/ncomms3244

Feng, Y., A. Ueda, and C.F. Wu. 2004. A modified minimal hemolymph-like solution, HL3.1, for physiological recordings at the neuromuscular junctions of normal and mutant Drosophila larvae. *J. Neurogenet.* 18:377–402. https://doi.org/10.1080/01677060490894522

Hanson, B.J., and W. Hong. 2003. Evidence for a role of SNX16 in regulating traffic between the early and later endosomal compartments. *J. Biol. Chem.* 278:34617–34630. https://doi.org/10.1074/jbc.M300143200

Herzog, J.J., M. Deshpande, L. Shapiro, A.A. Rodal, and S. Paradis. 2017. TDP-43 misexpression causes defects in dendritic growth. *Sci. Rep.* 7:15656. https://doi.org/10.1038/s41598-017-15914-4

Honbou, K., R. Minakami, S. Yuzawa, R. Takeya, N.N. Suzuki, S. Kamakura, H. Sumimoto, and F. Inagaki. 2007. Full-length p40phox structure suggests a basis for regulation mechanism of its membrane binding. *EMBO J.* 26:1176–1186. https://doi.org/10.1038/sj.emboj.7601561

Hoodless, P.A., T. Haerry, S. Abdollah, M. Stapleton, M.B. O'Connor, L. Attisano, and J.L. Wrana. 1996. MADR1, a MAD-related protein that functions in BMP2 signaling pathways. *Cell.* 85:489–500. https://doi.org/10.1016/S0092-8674(00)81250-7

Jansen, S., A. Collins, S.M. Chin, C.A. Ydenberg, J. Gelles, and B.L. Goode. 2015. Single-molecule imaging of a three-component ordered actin disassembly mechanism. *Nat. Commun.* 6:7202. https://doi.org/10.1038/ncomms8202

Kaksonen, M., and A. Roux. 2018. Mechanisms of clathrin-mediated endocytosis. *Nat. Rev. Mol. Cell Biol.* 19:313–326. https://doi.org/10.1038/nrm.2017.132

Kang, M.J., T.J. Hansen, M. Mickiewicz, T.J. Kaczynski, S. Fye, and S. Gunawardena. 2014. Disruption of axonal transport perturbs bone morphogenetic protein (BMP)--signaling and contributes to synaptic abnormalities in two neurodegenerative diseases. *PLoS One.* 9:e104617. https://doi.org/10.1371/journal.pone.0104617

Kelley, C.F., E.M. Messelaar, T.L. Eskin, S. Wang, K. Song, K. Vishnia, A.N. Becalska, O. Shupliakov, M.F. Hagan, D. Danino, et al. 2015. Membrane Charge Directs the Outcome of F-BAR Domain Lipid Binding and Autoregulation. *Cell Reports.* 13:2597–2609. https://doi.org/10.1016/j.celrep.2015.11.044

Kohl, J., J. Ng, S. Cachero, E. Ciabatti, M.J. Dolan, B. Sutcliffe, A. Tozer, S. Ruehle, D. Krueger, S. Frechter, et al. 2014. Ultrafast tissue staining with chemical tags. *Proc. Natl. Acad. Sci. USA.* 111:E3805–E3814. https://doi.org/10.1073/pnas.1411087111

Korkut, C., B. Ataman, P. Ramachandran, J. Ashley, R. Barria, N. Gherbesi, and V. Budnik. 2009. Trans-synaptic transmission of vesicular Wnt signals through Evi/Wntless. *Cell.* 139:393–404. https://doi.org/10.1016/j.cell.2009.07.051

Korkut, C., Y. Li, K. Koles, C. Brewer, J. Ashley, M. Yoshihara, and V. Budnik. 2013. Regulation of postsynaptic retrograde signaling by presynaptic exosome release. *Neuron.* 77:1039–1046. https://doi.org/10.1016/j.neuron.2013.01.013

Langemeyer, L., F. Fröhlich, and C. Ungermann. 2018. Rab GTPase Function in Endosome and Lysosome Biogenesis. *Trends Cell Biol.* 28:957–970. https://doi.org/10.1016/j.tcb.2018.06.007

Le Blanc, I., P.P. Luyet, V. Pons, C. Ferguson, N. Emans, A. Petiot, N. Mayran, N. Demaurex, J. Fauré, R. Sadoul, et al. 2005. Endosome-to-cytosol transport of viral nucleocapsids. *Nat. Cell Biol.* 7:653–664. https://doi.org/10.1038/ncb1269

Liao, E.H., L. Gray, K. Tsurudome, W. El-Mounzer, F. Elazzouzi, C. Baim, S. Farzin, M.R. Calderon, G. Kauwe, and A.P. Haghighi. 2018. Kinesin Khc-73/KIF13B modulates retrograde BMP signaling by influencing endosomal dynamics at the *Drosophila* neuromuscular junction. *PLoS Genet.* 14:e1007184. https://doi.org/10.1371/journal.pgen.1007184

Lorenzo, D.N., A. Badea, J. Davis, J. Hostettler, J. He, G. Zhong, X. Zhuang, and V. Bennett. 2014. A PIK3C3-ankyrin-B-dynactin pathway promotes axonal growth and multiorganelle transport. *J. Cell Biol.* 207:735–752. https://doi.org/10.1083/jcb.201407063

Lucas, M., D.C. Gershlick, A. Vidaurrazaga, A.L. Rojas, J.S. Bonifacino, and A. Hierro. 2016. Structural Mechanism for Cargo Recognition by the Retromer Complex. *Cell.* 167:1623–1635.

Markstein, M., C. Pitsouli, C. Villalta, S.E. Celniker, and N. Perrimon. 2008. Exploiting position effects and the gypsy retrovirus insulator to engineer precisely expressed transgenes. *Nat. Genet.* 40:476–483. https://doi.org/10.1038/ng.101

Marqués, G., H. Bao, T.E. Haerry, M.J. Shimell, P. Duchek, B. Zhang, and M.B. O'Connor. 2002. The *Drosophila* BMP type II receptor Wishful Thinking regulates neuromuscular synapse morphology and function. *Neuron.* 33: 529–543. https://doi.org/10.1016/S0896-6273(02)00595-0

McCabe, B.D., G. Marqués, A.P. Haghighi, R.D. Fetter, M.L. Crotty, T.E. Haerry, C.S. Goodman, and M.B. O'Connor. 2003. The BMP homolog Gbb provides a retrograde signal that regulates synaptic growth at the *Drosophila* neuromuscular junction. *Neuron.* 39:241–254. https://doi.org/10.1016/S0896-6273(03)00426-4

McMahon, H.T., and E. Boucrot. 2015. Membrane curvature at a glance. *J. Cell Sci.* 128:1065–1070. https://doi.org/10.1242/jcs.114454

McMahon, H.T., and J.L. Gallop. 2005. Membrane curvature and mechanisms of dynamic cell membrane remodelling. *Nature.* 438:590–596. https://doi.org/10.1038/nature04396

Pan, B.T., and R.M. Johnstone. 1983. Fate of the transferrin receptor during maturation of sheep reticulocytes in vitro: selective externalization of the receptor. *Cell.* 33:967–978. https://doi.org/10.1016/0092-8674(83)90040-5

Persson, U., H. Izumi, S. Souchelnytskyi, S. Itoh, S. Grimsby, U. Engström, C.H. Heldin, K. Funa, and P. ten Dijke. 1998. The L45 loop in type I receptors for TGF-beta family members is a critical determinant in specifying Smad isoform activation. *FEBS Lett.* 434:83–87. https://doi.org/10.1016/S0014-5793(98)00954-5

Pylypenko, O., R. Lundmark, E. Rasmuson, S.R. Carlsson, and A. Rak. 2007. The PX-BAR membrane-remodeling unit of sorting nexin 9. *EMBO J.* 26: 4788–4800. https://doi.org/10.1038/sj.emboj.7601889

Rajendran, L., H.J. Knölker, and K. Simons. 2010. Subcellular targeting strategies for drug design and delivery. *Nat. Rev. Drug Discov.* 9:29–42. https://doi.org/10.1038/nrd2897

Rawson, J.M., M. Lee, E.L. Kennedy, and S.B. Selleck. 2003. *Drosophila* neuromuscular synapse assembly and function require the TGF-beta type I receptor saxophone and the transcription factor Mad. *J. Neurobiol.* 55: 134–150. https://doi.org/10.1002/neu.10189

Rodal, A.A., A.D. Blunk, Y. Akbergenova, R.A. Jorquera, L.K. Buhl, and J.T. Littleton. 2011. A presynaptic endosomal trafficking pathway controls synaptic growth signaling. *J. Cell Biol.* 193:201–217. https://doi.org/10.1083/jcb.201009052

Satoh, A.K., J.E. O'Tousa, K. Ozaki, and D.F. Ready. 2005. Rab11 mediates post-Golgi trafficking of rhodopsin to the photosensitive apical membrane of *Drosophila* photoreceptors. *Development.* 132:1487–1497. https://doi.org/10.1242/dev.01704

Schindelin, J., I. Arganda-Carreras, E. Frise, V. Kaynig, M. Longair, T. Pietzsch, S. Preibisch, C. Rueden, S. Saalfeld, B. Schmid, et al. 2012. Fiji: an open-source platform for biological-image analysis. *Nat. Methods.* 9: 676–682. https://doi.org/10.1038/nmeth.2019

Scott-Solomon, E., and R. Kuruvilla. 2018. Mechanisms of neurotrophin trafficking via Trk receptors. *Mol. Cell. Neurosci.* 91:25–33. https://doi.org/10.1016/j.mcn.2018.03.013

Shin, H.W., M. Hayashi, S. Christoforidis, S. Lacas-Gervais, S. Hoepfner, M.R. Wenk, J. Modregger, S. Uttenweiler-Joseph, M. Wilm, A. Nystuen, et al. 2005. An enzymatic cascade of Rab5 effectors regulates phosphoinositide turnover in the endocytic pathway. *J. Cell Biol.* 170:607–618. https://doi.org/10.1083/jcb.200505128

Smith, R.B., J.B. Machamer, N.C. Kim, T.S. Hays, and G. Marqués. 2012. Relay of retrograde synaptogenic signals through axonal transport of BMP receptors. *J. Cell Sci.* 125:3752–3764. https://doi.org/10.1242/jcs.094292

Stachowiak, J.C., C.C. Hayden, and D.Y. Sasaki. 2010. Steric confinement of proteins on lipid membranes can drive curvature and tubulation. *Proc. Natl. Acad. Sci. USA.* 107:7781–7786. https://doi.org/10.1073/pnas.0913306107

Stachowiak, J.C., E.M. Schmid, C.J. Ryan, H.S. Ann, D.Y. Sasaki, M.B. Sherman, P.L. Geissler, D.A. Fletcher, and C.C. Hayden. 2012. Membrane bending by protein-protein crowding. *Nat. Cell Biol.* 14:944–949. https://doi.org/10.1038/ncb2561

Strigini, M., and S.M. Cohen. 2000. Wingless gradient formation in the *Drosophila* wing. *Curr. Biol.* 10:293–300. https://doi.org/10.1016/S0960-9822(00)00378-X

Teasdale, R.D., and B.M. Collins. 2012. Insights into the PX (phox-homology) domain and SNX (sorting nexin) protein families: structures, functions and roles in disease. *Biochem. J.* 441:39–59. https://doi.org/10.1042/BJ20111226

van Weering, J.R., R.B. Sessions, C.J. Traer, D.P. Kloer, V.K. Bhatia, D. Stamou, S.R. Carlsson, J.H. Hurley, and P.J. Cullen. 2012. Molecular basis for SNX-BAR-mediated assembly of distinct endosomal sorting tubules. *EMBO J.* 31:4466–4480. https://doi.org/10.1038/emboj.2012.283

Wills, R.C., B.D. Goulden, and G.R.V. Hammond. 2018. Genetically encoded lipid biosensors. *Mol. Biol. Cell.* 29:1526–1532. https://doi.org/10.1091/mbc.E17-12-0738

Xia, Z., H. Dudek, C.K. Miranti, and M.E. Greenberg. 1996. Calcium influx via the NMDA receptor induces immediate early gene transcription by a MAP kinase/ERK-dependent mechanism. *J. Neurosci.* 16:5425–5436. https://doi.org/10.1523/JNEUROSCI.16-17-05425.1996

Xu, J., L. Zhang, Y. Ye, Y. Shan, C. Wan, J. Wang, D. Pei, X. Shu, and J. Liu. 2017. SNX16 Regulates the Recycling of E-Cadherin through a Unique Mechanism of Coordinated Membrane and Cargo Binding. *Structure.* 25: 1251–1263.

Ye, M., K.M. Lehigh, and D.D. Ginty. 2018. Multivesicular bodies mediate long-range retrograde NGF-TrkA signaling. *eLife.* 7:e33012. https://doi.org/10.7554/eLife.33012

Zeno, W.F., U. Baul, W.T. Snead, A.C.M. DeGroot, L. Wang, E.M. Lafer, D. Thirumalai, and J.C. Stachowiak. 2018. Synergy between intrinsically disordered domains and structured proteins amplifies membrane curvature sensing. *Nat. Commun.* 9:4152. https://doi.org/10.1038/s41467-018-06532-3

Zhang, L., D. Qin, C. Hao, X. Shu, and D. Pei. 2013. SNX16 negatively regulates the migration and tumorigenesis of MCF-7 cells. *Cell Regen. (Lond.).* 2:3.